Urban Climate 65 (2026) 102779

Contents lists available at ScienceDirect

Urban Climate

journal homepage: www.elsevier.com/locate/uclim

Analysis of urban thermal structures in different scenarios of hot weather: The Bologna case study

Marco Possega *, Erika Brattich, Carlo Cintolesi, Paolo Ruggieri, Silvana Di Sabatino

Department of Physics and Astronomy "Augusto Righi", University of Bologna, via Irnerio 46, Bologna, 40126, Italy

ARTICLE INFO

Keywords:
Urban heat island
Climate scenarios
High-resolution simulations
Thermal structure

ABSTRACT

It is recognized that in summer many urban areas increasingly experience days of extreme heat caused by a combination of regional climate change and local effects due to the Urban Heat Island (UHI). Southern Europe, particularly the Po Valley region in Italy, faces several challenges such as land degradation, rapid urbanization, and intensifying climate impacts, with Bologna exemplifying the intricate interplay between these risk factors. Here, high-resolution Weather Research and Forecasting (WRF) model simulations are employed to investigate the three-dimensional urban thermal dynamics under present and future projected extreme heat scenarios. A multi-scale modeling framework is applied to simulate representative Hot Weather (HW) events in the near and far future under two emission scenarios (SSP245 and SSP585), along with a present-day reference event. Results show that the UHI effect persists in all cases and intensifies during HW periods, especially at night. HW events induce strong near-surface warming, with a persistent urban–rural temperature contrast of about 3–5 °C and an upward shift of the 30 °C isotherm, while simultaneously compressing the UHI vertically from ~250 m in present conditions to ~100–140 m in future HW scenarios. Scenario-dependent differences emerge, especially in the far future: SSP585 leads to stronger and more persistent nocturnal overheating, slower recovery, and deeper atmospheric warming, whereas SSP245 shows more moderate, rapidly reversible UHI anomalies with a more regular diurnal cycle. This study highlights the importance of a three-dimensional diagnostic approach and underscores the role of emission pathways in modulating future urban heat stress.

1. Introduction

Urbanization profoundly alters land–atmosphere interactions by modifying surface properties, energy fluxes, and hydrological processes (Pielke Sr et al., 2011; Bounoua et al., 2002). The replacement of natural landscapes with artificial surfaces changes local and regional climate through reduced evapotranspiration, increased heat storage, and altered radiative and aerodynamic characteristics (Collier, 2006; Oke, 1980; Mouzourides et al., 2019). As a result, urban areas typically experience higher temperatures than their rural surroundings — a phenomenon known as the Urban Heat Island (UHI) effect — driven by urban geometry, material properties, and anthropogenic heat emissions (Oke et al., 2017; Phelan et al., 2015; Biagi et al., 2025; Gonzalez-Trevizo et al., 2021). These processes vary across cities and seasons depending on factors such as population density, land use, and regional climate, thus shaping distinct urban thermal environments (Manoli et al., 2019).

* Correspondence to: Institute of Atmospheric Sciences and Climate (CNR-ISAC), Via Gobetti 101, Bologna, 40129, Italy.
E-mail address: marcopossega@cnr.it (M. Possega).

https://doi.org/10.1016/j.uclim.2026.102779
Received 8 August 2025; Received in revised form 22 December 2025; Accepted 10 January 2026
Available online 16 January 2026

Extreme heat events further exacerbate urban warming, amplifying health risks and infrastructure stress (Luber and McGeehin, 2008). Major heatwaves, such as those in Europe in 2003 and Russia in 2010, have demonstrated the high vulnerability of urban populations to extreme temperatures (Lee, 2014). With projections indicating more frequent, intense, and prolonged heatwaves under future climate scenarios (Perkins et al., 2012), understanding their influence on urban thermal structures has become increasingly urgent for effective adaptation and mitigation strategies.

Thermal structures in urban contexts are investigated through ground-based observations, remote sensing, and numerical simulations at various spatial and temporal scales. Each method has specific limitations: ground-based measurements provide detailed local data but lack spatial coverage (Fabrizi et al., 2010), whereas remote sensing ensures wide spatial representation but is affected by cloud cover, inconsistent urban definitions, and spatio-temporal gaps (Diem et al., 2024; Voogt and Oke, 2003). To overcome these constraints, numerical simulations — particularly with the Weather Research and Forecasting (WRF) model — allow flexible resolution and controlled experimentation on how urban form and function interact with climate (Giannaros et al., 2013). WRF coupled with urban canopy models has been widely used to assess the effects of urbanization and anthropogenic heat on local climates (Mughal et al., 2020), showing, for example, temperature increases up to 2 °C in urban China due to urbanization and heat emissions (Feng et al., 2012), or cooling effects from enhanced evapotranspiration under optimized irrigation schemes (Yang and Wang, 2015). High-resolution setups can distinguish intra-urban UHIs beyond satellite capabilities (Di Sabatino et al., 2020), and their performance improves markedly with advanced urban parameterizations and updated land cover data (Li et al., 2020). However, despite extensive research, significant gaps remain in our understanding of the influence of extreme heat on urban areas (Kong et al., 2021). The findings of existing studies are conflicting, and an increase in UHI under extreme heat conditions — and consequently in a warming future scenario — is not necessarily guaranteed (Scott et al., 2018; Chew et al., 2021; Richard et al., 2021). In addition, most of the research in this field focuses on American and Asian cities (Roberge and Sushama, 2018; Rosenzweig et al., 2005; Ma et al., 2022; Sharma et al., 2019), whose urban morphology differs significantly from that of European cities (Antipova, 2018; Huang et al., 2007). Southern Europe, though being among the regions most vulnerable to severe threats — including land degradation, rapid urbanization, and the projected extreme impacts of climate change —, remains a relatively under-explored area. Few studies have analyzed the urban heat island under future climate scenarios in this region, and even fewer have investigated its vertical structure. High-resolution WRF-ARW simulations for Rome and Thessaloniki indicate potential UHI changes under RCP8.5 by the end of the century (Keppas et al., 2021), while CORDEX-SURFEX-TEB projections for Lisbon show increasing frequency of extreme hot days and nights, though with roughly constant UHI magnitude across hours and urban/rural areas (Nogueira et al., 2020). Broader European studies using high-resolution modeling highlight potential temperature-related trends in cities like Genova, Eindhoven, and Tampere (Ascenso et al., 2024), yet these generally do not assess vertical UHI profiles. Similarly, multi-model climate projections for Swiss cities indicate a strong increase in urban heat extremes compared to rural areas, particularly during night-time, but vertical UHI characteristics remain unexplored (Burgstall et al., 2021). According to a recent review (Zhu and Ooka, 2023), existing projections have primarily explored the effects of urban expansion or mitigation strategies such as green and cool roofs under RCP-based climate scenarios (Argüeso et al., 2014; Tewari et al., 2019; Rafael et al., 2016; Doan and Kusaka, 2018), often predicting substantial increases in urban temperature and human heat stress toward mid- and late-21st century conditions. However, these studies mostly focus on surface temperature changes, while the investigation of the vertical thermal structure of UHIs — and its evolution under distinct socio-economic scenarios — remains largely unexplored. Most of these studies focus on single future RCP (or SSP) scenarios and rarely compare multiple SSPs, limiting the understanding of how alternative socio-economic pathways may influence future urban heat dynamics.

The study of the thermal vertical and horizontal structure in urban contexts under different future scenarios is crucial for developing effective urban planning and climate adaptation strategies (Keppas et al., 2021), and it is also essential for mitigating the adverse effects of urbanization and climate change (Ascenso et al., 2024). The vertical structure, encompassing the distribution of temperature at various heights, affects atmospheric stability and pollutant dispersion, which are critical for air quality and public health (Ching, 2013). The horizontal structure, which includes surface temperature variations across different urban areas, influences local weather patterns and can exacerbate heat stress in densely populated regions (Lemonsu et al., 2015). To consider the various environmental conditions impacting the future climate, Kriegler et al. (2012) introduces the use of socio-economic scenarios in climate change analysis, discussing the concept of Shared Socio-economic Pathways (SSPs). These scenarios are important for understanding the interplay between socio-economic development and climate change impacts, including extreme heat.

This study aims to address the impacts of distinct SSPs on modifying the thermal structure of a South-European historical city, i.e. Bologna, and to examine the variation of the three-dimensional thermal structure of urban areas under projected extreme heat conditions. Building upon the methodology established by Silva et al. (2022) and utilizing a state-of-the-art model for high-resolution dynamical downscaling, this research is based on the analysis of one control (present) simulation and four future simulations under different SSP scenarios. By integrating horizontal and vertical analyses, this work addresses two key questions:

- What are the variations in the three-dimensional thermal structure of urban areas between current and projected extreme heat conditions?
- How is the thermal structure of a historical South-European city influenced under climate conditions associated with different Shared Socioeconomic Pathway (SSP) scenarios?

This study is structured as follows: Section 2 provides a detailed description of the study area and the methodology to select the events to investigate under the different scenarios, along with the employed dataset and the setup for the simulations performed in the analysis. Section 3 outlines the model validation and the results obtained for the control case of the August 2023 heatwave. Then, it presents the resulting temperature patterns and the characteristics of thermal structure in Bologna during the projected extreme heat events, comparing the outcomes belonging to different scenarios. Finally, Conclusions summarize the key insights and suggesting directions for future research.

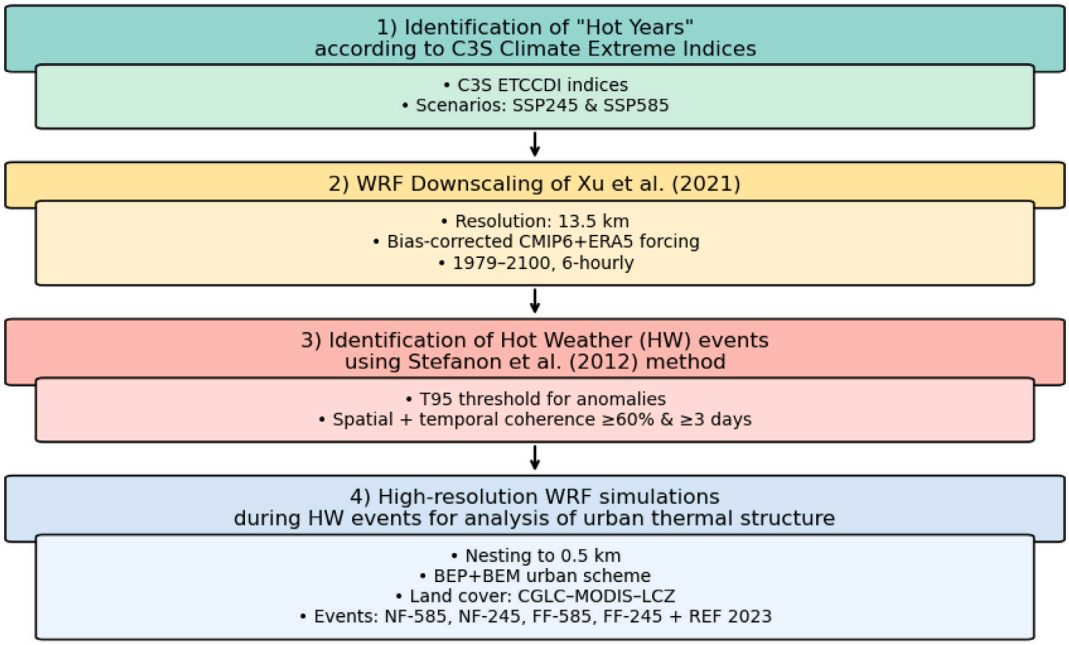

Fig. 1. Schematic representation of the multi-scale workflow implemented in this study.

2. Materials and methods

A methodology for analyzing the UHI effect in future scenarios is developed and applied to the case study of the city of Bologna, Italy (44.49N, 11.34E, 54 m asl). Located in the Po Valley and bordered to the south by the Apennines Mountains, Bologna is the seventh most populous city in the country (with a population of around 400,000 inhabitants) and a relatively large medieval historical center. The city experiences a humid subtropical climate (Cfa) according to the Köppen and Geiger climate classification (Kottek et al., 2006), characterized by hot summers with temperatures frequently exceeding 38 °C, limited nocturnal cooling, and frequent temperature inversions, particularly in summer and winter (Rossa et al., 2020). The city is recognized as a climate change hotspot (Straffelini and Tarolli, 2023), also due to the prevailing weather conditions characterized by weak winds and poor ventilation in urban neighborhoods (Jongen and Bonafè, 2006). These peculiarities make Bologna a particularly interesting case study for the analysis of the UHI phenomenon, which can also benefit from a well-documented literature on urban climate modeling (Nardino et al., 2022; Cremonini et al., 2023) and large observational datasets (Valmassoi et al., 2020).

The present study utilizes a multi-scale approach to investigate urban responses to extreme heat events in future climatic scenarios. First, climatic projections on the near (2025–2049) and far (2075–2100) future are analyzed to identify "hot years", by analyzing key climate indicators under different socio-environmental scenarios (see Section 2.1). Second, climatic projections of selected "hot years" are downscaled to medium-resolution (13.5 km spatial resolution) utilizing the WRF model to identify summer hot weather events, i.e. sub-annual periods (typically one or a few weeks) of extreme heat (see Section 2.2). Third, WRF high-resolution simulations (0.5 km resolution) are carried out to reproduce in detail the weather events and analyze the UHI effects in his period (see Section 2.3). The above-mentioned steps are schematized in Fig. 1 and are described in detail in the following sections.

2.1. Identification of future hot years

To identify years with a high probability of extreme heat events based on the two SSP585 (business-as-usual) and SSP245 (mitigation policies) scenarios, we used the Copernicus Climate Change Service (C3S) dataset (Sandstad et al., 2022), which provides climate extreme indices derived from CMIP6 (Eyring et al., 2016) model ensembles. These indices, suggested by the Expert Team on Climate Change Detection and Indices (Karl et al., 1999), characterize the occurrence of temperature and precipitation extremes rather than absolute near-surface temperatures, resulting in a total of 126 time series for each index. The following ones are selected for the present study:

- Warm Days (TX90p): Percentage of days with maximum temperature exceeding the 90th percentile within a 5-day window (1981–2010 climatology);
- Warm Nights (TN90p): Percentage of days with minimum temperature exceeding the 90th percentile within a 5-day window (1981–2010 climatology);

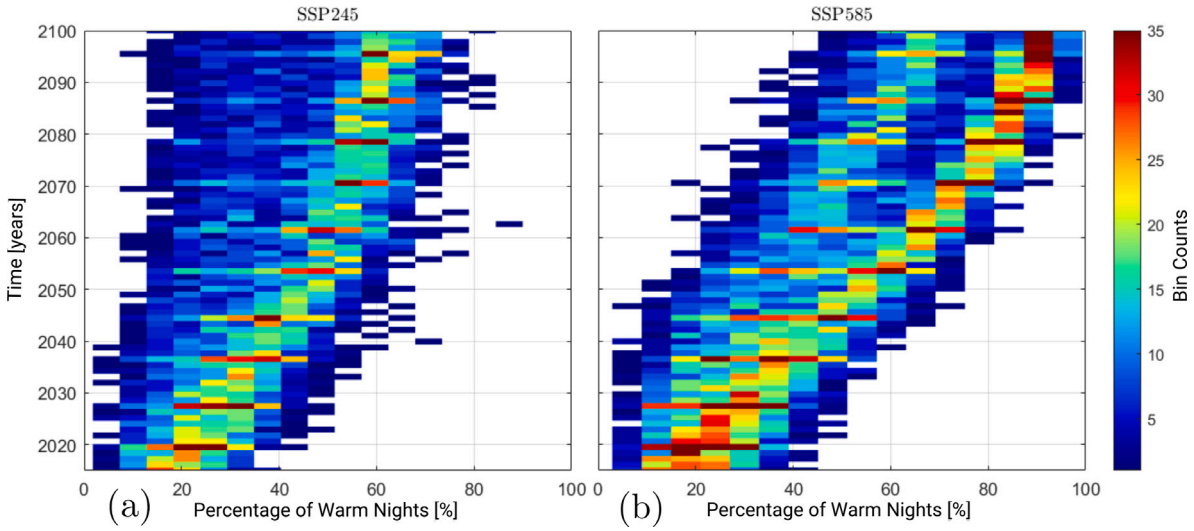

Fig. 2. Binned scatterplots of TN90p (Warm Nights) according to C3S data for SSP585 (a) and SSP245 (b) scenarios for Bologna.

Table 1
Selected "hot years" with corresponding scenarios, categorized by period, including values of chosen TN90p threshold ($TN90_{thr}$) and bin counts above that threshold (Bin_{thr}).

Label	Year	Scenario	Period	$TN90_{\mathrm{thr}}$	Bin_{thr}
NF-585	2033	SSP585	Near future	30%	77/126
NF-245	2037	SSP245	Near future	30%	75/126
FF-585	2082	SSP585	Far future	50%	98/126
FF-245	2087	SSP245	Far future	50%	94/126

- Summer Days (SU): Annual count of days with maximum temperature above 25 °C.

Fig. 2 shows the yearly value of the TN90p index predicted in the SSP585 and SSP245 scenarios, in the grid cell covering Bologna. They are plotted as a binned scatter plot to visualize trends and identify periods with the highest probability of extreme heat events. The comparison between the two scenarios reveals that SSP585 shows a significant increase in the percentage of warm nights, with two distinct evolution patterns among ensemble members indicating a higher likelihood of extreme heat events. Conversely, SSP245 suggests a stabilization in warm extremes, with a narrower range of values, consistently with the IPCC assessment (Shukla et al., 2022). The same analyses have been done for the other two indices, which revealed similar behaviors.

By analyzing the behavior of TN90p index separately for near future (2025–2049) and far future (2075–2100) projections, the years with the highest likelihood of extreme heat events under the two SSP scenarios are identified. Specifically, years in which more than half of the 126 time series show warm night percentages exceeding the 50% TN90p threshold ($TN90_{thr}$) for the far future and 30% for the near future are identified. The use of different thresholds for the two periods reflects the progressive increase in both the number and relative frequency of warm nights projected in the future. As illustrated in both SSP585 and SSP245 scenarios (Fig. 2) and noted earlier, warm nights are expected to rise steadily until around 2050, after which the two scenarios diverge: SSP245 tends to stabilize, while SSP585 continues to increase. Adopting distinct thresholds for the near and far future, thus, allows focusing on periods of heightened heat and provides a more consistent comparison of climate indicators across different time frames and emission pathways. Based on this criterion, 2033 (SSP585) and 2037 (SSP245) are selected as the "hot years" for the near future, and 2082 (SSP585) and 2087 (SSP245) for the far future (See Table 1). These selections represent periods with high extreme-heat probability, facilitating targeted analyses of urban responses under different socio-environmental scenarios. Although these "hot years" do not correspond to specific calendar years, they serve as reference periods for studying evolving thermal patterns and their implications for climate resilience in Bologna.

2.2. Climate projection downscaling with WRF

Dynamical downscaling is a powerful tool for representing complex climatic conditions at regional and sub-regional scales, but uncertainties arise primarily from the use of boundary conditions provided by General Circulation Models, which are subject to biases (Tapiador et al., 2020; Latif, 2013). To address this, the bias-corrected dataset of Xu et al. (2021) combines CMIP6 projections (Eyring et al., 2016) with ERA5 reanalysis data (Hersbach et al., 2020), producing a consistent set of surface and

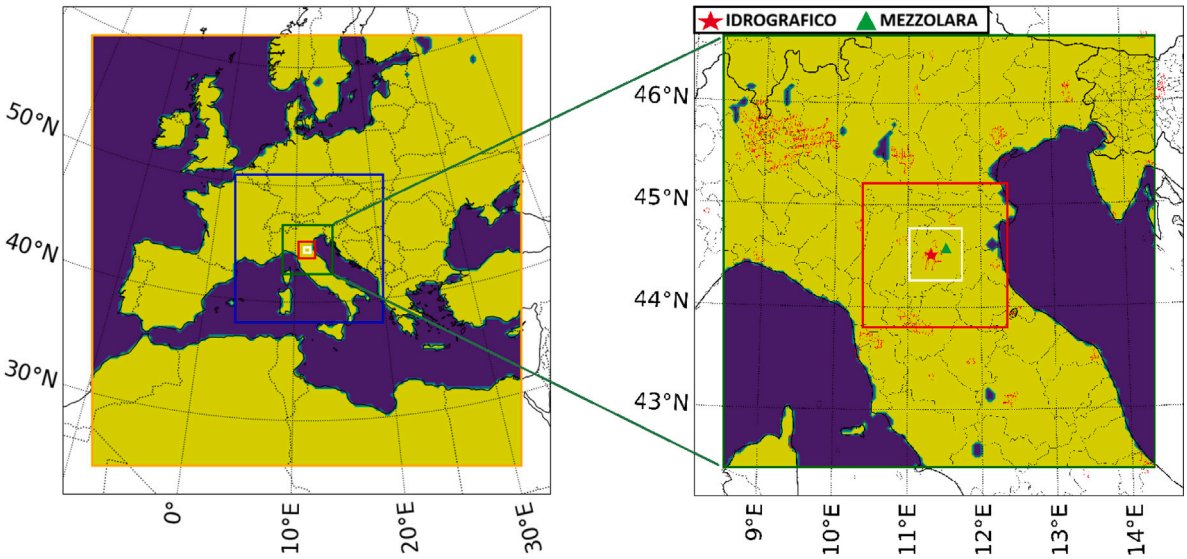

Fig. 3. Left: the 5-nested domains for high resolution WRF simulations over Bologna (left): orange box for D01 40.5 km, blue box for D02 13.5 km, green box for D03 4.5 km, red box for D04 1.5 km and white box for D05 0.5 km. Right: zoom on the D04 (red box, 1.5 km resolution) and D05 (white box, 0.5 km resolution) domains for the high resolution WRF simulations over Bologna, with markers indicating the urban Bologna Idrografico (red) and rural Mezzolara (green) in-situ weather stations.

upper-air variables that serve as initial and boundary conditions for high-resolution WRF simulations. The dataset spans 1979–2100 under SSP245 and SSP585 scenarios, with a spatial resolution of 1.25° and six-hourly intervals, and preserves internal climate variability while incorporating non-linear trends from the CMIP6 ensemble, ensuring physically consistent conditions for dynamical downscaling.

WRF simulations are carried out with five two-way nested domains with 100 × 100, 103 × 103, 103 × 103, 103 × 103, and 112 × 112 grid cells, with resolution of 40.5, 13.5, 4.5, 1.5 and 0.5 km respectively, centered in Bologna, Italy (Fig. 3).

To maintain consistency with previous research, the same parameterization schemes adopted by Zonato et al. (2020) for evaluating the UHI of Bologna are here employed. Specifically, the simulation uses the state-of-the-art urban parameterization in WRF, namely the Building Effect Parameterization coupled to the Building Energy Model (BEP+BEM) scheme (Salamanca et al., 2010), together with land surface model (Niu et al., 2011) is adopted. In this configuration, anthropogenic heat fluxes are computed dynamically from building energy use rather than prescribed values: BEM simulates heat released by heating, ventilation and air conditioning systems, heat generated inside buildings from people (metabolic heat), lighting, and electrical equipment, while BEP vertically distributes this heat within the urban canopy. The resulting flux is added as a sensible heat source in the surface energy balance, influencing the urban boundary layer and contributing to the urban heat island effect. This parameterization can also enhance the nocturnal UHI by sustaining higher night-time temperatures through the delayed release of heat stored in buildings and urban surfaces. The default resolution of WRF datasets for land use and topography (30”) is too coarse for our sub-kilometer-scale simulations. Therefore, the hybrid 100-m global CGLC–MODIS–LCZ land cover dataset developed by Demuzere et al. (2023) is used (see Fig. 4). For topographical data, the high-resolution SRTM (Shuttle Radar Topography Mission) dataset with a 100-meter resolution is utilized, as detailed in Siewert and Kroszczynski (2020). In terms of vertical resolution, 51 vertical η levels (terrain-following hydrostatic-pressure coordinates) are selected, with a focus on the first 100 m from the surface, which includes 7 vertical levels. This configuration is considered effective for capturing extreme weather events at the urban scale, as it combines advanced urban parameterization, high-resolution land cover and topography, and enhanced vertical resolution near the surface. It allows for an accurate representation of urban-atmosphere interactions, essential for assessing climate change impacts in cities.

2.3. Identification of projected “Hot Weather events”

The final step of the methodology consists in assessing the impact of projected periods of high temperatures on the thermal structure of Bologna under various scenarios, using the output of WRF simulations. Taking inspiration by Wang et al., these events are named “Hot Weather events” (HW), which is a more flexible and inclusive definition than “extreme heat” or “heatwaves”. Extreme heat is typically defined as exceptionally high temperatures that exceed regional and seasonal norms, posing significant risks to human health, infrastructure, and ecosystems (Horton et al., 2016). This term often lacks a specific temporal or spatial definition, which is crucial for consistent climate analysis. Heatwaves are generally understood as prolonged periods of unusually high temperatures, often spanning several days or weeks (Robinson, 2001). While heatwaves have clearer definitions, they may exclude shorter but equally impactful temperature spikes. Given the downscaled nature of the climate projection dataset and the

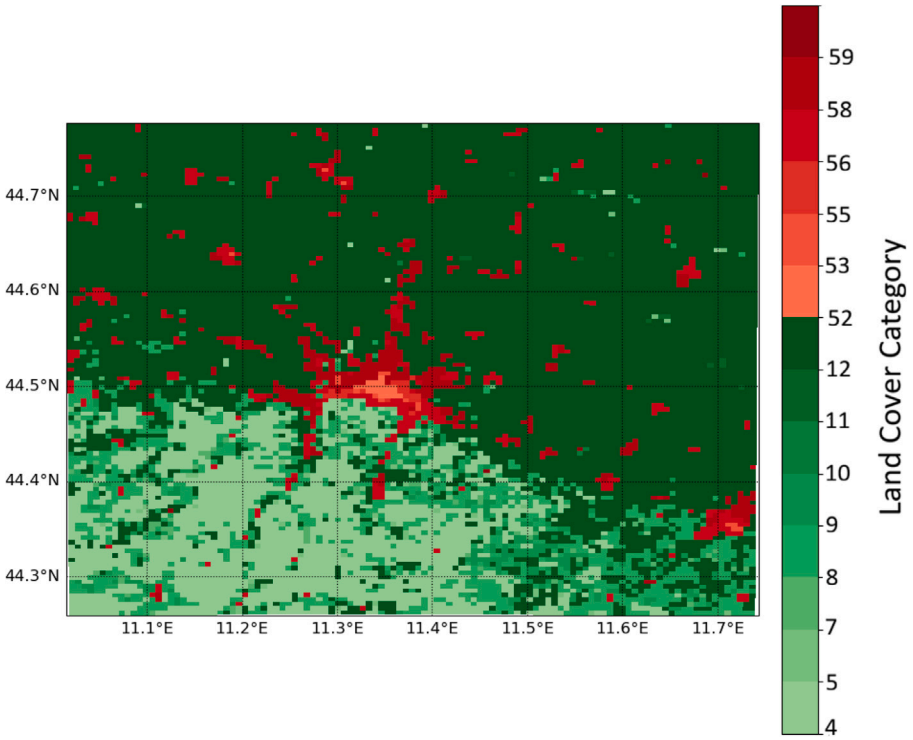

Fig. 4. The hybrid 100-m global CGLC–MODIS–LCZ land cover map for domain D05. Red areas refer to urban classes, while green areas refer to rural.

Table 2
Selected "Hot Weather (HW) events" for each corresponding scenarios, with respective HW days and study period.

Label	Year	Scenario	HW Event	Study Period
REF	2023	historical	21–26 August	16–31 August
NF-585	2033	SSP585	11–14 June	6–19 June
NF-245	2037	SSP245	23–28 August	18 August–2 September
FF-585	2082	SSP585	30 August–10 September	25-August–15 September
FF-245	2087	SSP245	12–16 June	7–21 June

need to identify events across diverse future scenarios, the term "hot weather" strikes a balance between specificity and inclusivity. It encompasses both sudden, acute spikes in temperature and longer, sustained periods of heat, thereby enabling the identification of thermally relevant events without relying on rigid, context-dependent definitions such as "heatwave" (WMO, 2015).

HW events have been identified by analyzing the climatological mean distribution of temperature for the reference period 2000–2022, following the approach proposed by Stefanon et al. (2012). The aim is to establish robust and consistent thresholds for identifying HW events under the current and future climate while accounting for evolving temperature extremes over time. Using hourly temperature outputs from the WRF model at 13.5 km resolution described in Section 2.2, daily temperature anomalies are calculated for each grid point relative to the 2000–2022 climatology derived from ERA5 reanalysis. Following Perkins (2015), days are classified as extremely hot when temperature anomalies exceed the 95th percentile (T95) of the local probability density function. The use of the T95 threshold suggested by Stefanon et al. (2012) is also widely adopted in heatwave detection studies in different areas of the world (Anderson and Bell, 2009; Tong et al., 2010; Xu et al., 2013; Zeng et al., 2014; Zhang et al., 2015; Ma et al., 2015; Possega et al., 2022) and ensures that only the most extreme and persistent events are captured. Using a lower percentile threshold (e.g., the 90th) would increase the number of detected events, though it would reduce the focus on the most severe heat extremes. The T95 threshold is calculated using a 21-day centered moving average across the reference climatology, balancing the detection of significant events with statistical reliability. To ensure spatial coherence and filter out isolated anomalies, it is required that at least 60% of a 25 × 25 cell centered on Bologna exceeds the T95 threshold. This condition must persist for at least 3 consecutive days, with all such days within the period classified as HW days. The analysis centers on four identified events: two near-future events (NF-585 and NF-245) and two far-future events (FF-585 and FF-245), compared against a baseline August 2023 heatwave event (hereafter labeled as REF, see Table 2).

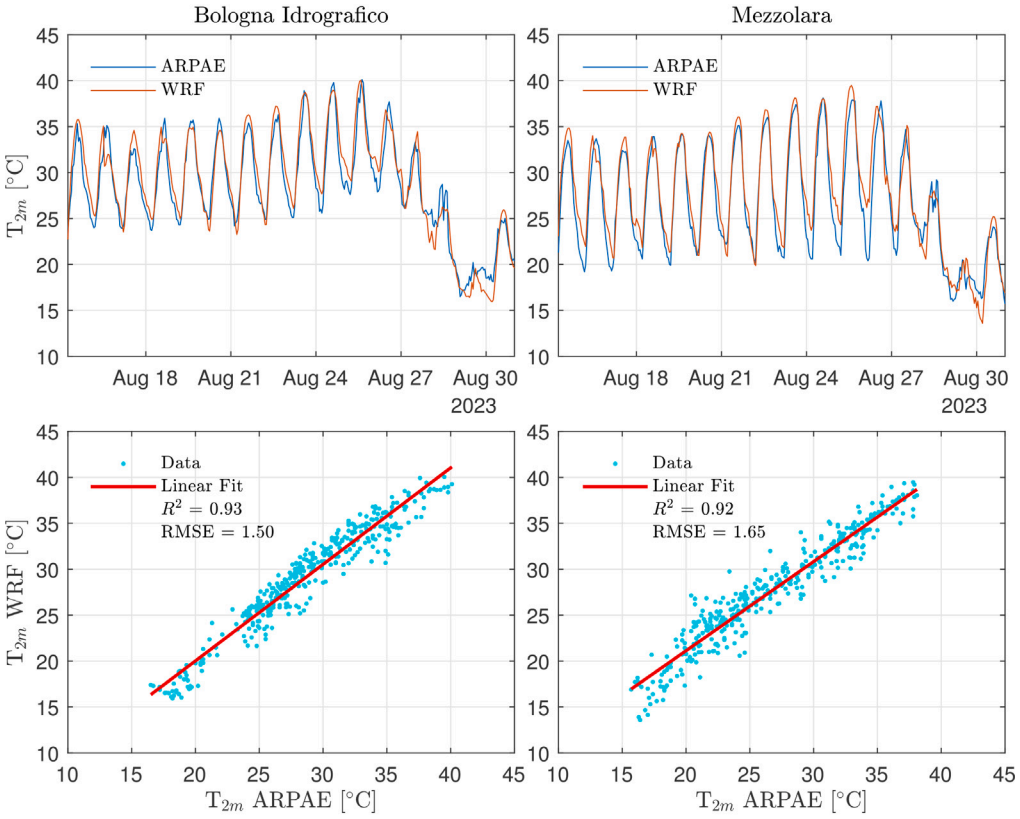

Fig. 5. Validation of WRF simulation with observed T_{2m} (temperature at 2 m from the ground) values, distinguishing urban (Bologna Idrografico) and rural (Mezzolara) ARPAE stations.

3. Results and discussion

3.1. Control case

The simulation approach and settings have been assessed by reproducing the control case on a heatwave impacting the whole Italian peninsula during the summer of 2023. Initial and boundary conditions are derived from the ERA5 reanalysis dataset, enabling a nested domain structure streamlined from 13.5 km to 0.5 km. Considering the HW event from 21 to 26 August 2023, the simulation covers a period starting six days before the heatwave onset, allowing for one day of model spin-up, and extends to five days after the heatwave ends, therefore covering the interval 16–31 August 2023.

3.1.1. Model validation with observations

The numerical outputs of the simulation are validated comparing against open source observational data collected by meteorological stations of the Regional Agency for Prevention, Environment and Energy of Emilia Romagna (ARPAE, 2023). The average 2 m air temperature (T_{2m}) reproduced by the WRF simulation with the highest resolution (0.5 km) are compared with measurements at two selected locations: Bologna Idrografico (44.50N, 11.35E, 84 m asl) and Mezzolara (44.57N, 11.53E, 20 m asl), respectively located in the Bologna urban and rural area (see markers in Fig. 3).

Fig. 5 shows the temporal series of observed and simulated T_{2m} at both locations, along with scatter plots showcasing the linear regression between simulated and observed values. Overall, the simulations reproduce the daily temperature variation in good agreement with the measurements. In both locations, a slight overestimation of the night-time temperature is detectable in the period 23–26 August. This nocturnal bias is a well-documented feature of WRF under stable boundary-layer conditions (Giannaros et al., 2013; Lin et al., 2016; Bhati and Mohan, 2018; Salamanca et al., 2018; Vogel and Afshari, 2020), particularly in urban areas, where excessive heat storage and reduced nocturnal cooling can lead to warmer simulated night-time temperatures. The effect is primarily attributed to the parameterization of urban canopy and surface energy balance, which can overestimate the retention of heat within built environments. However, this overestimation remains within an acceptable range ($RMSE < 2$°C) and does not significantly compromise the ability of the simulation to capture the observed temperature pattern or the relative UHI intensity between urban and rural sites. Also, the very high correlation between observations and simulations ($R^2 > 0.9$) confirms that the control case produces reliable results.

3.1.2. Thermal structure above the urban area in the present scenario

The urban thermal structure of the control case is analyzed for the period 16–31 August 2023. The first two aspects examined are the temporal evolution of the average 2 m air temperature (T_{2m}) in Bologna urban and rural areas, and the modification of the vertical thermal structure above the urban area of Bologna, analyzed through the time–height cross section of temperature.

Fig. 6a displays the temporal evolution of T_{2m} over Bologna, distinguishing between spatial averages over urban and rural areas spanning from 16 to 31 August 2023, with time given in UTC (local time = UTC+2). Considering land cover classification provided in Demuzere et al. (2023) and reported in Fig. 4, urban temperature T_U is calculated by averaging over urban land cover classes (categories 52–59) within the area (44.4–44.6°N, 11.2–11.45°E), whereas rural temperature (T_R) is computed by averaging over rural land cover classes (categories 4–12) outside this area. Fig. 6a also describes the modification of the UHI index (represented by the dashed blue line), defined as $T_U - T_R$ (Basara et al., 2008). Both temperature series exhibit a regular diurnal cycle, with daily temperature maxima occurring around 12:00 UTC (14:00 local time), and minima around 03:00 UTC (05:00 local time). Urban temperatures are systematically higher than rural ones (+0.5 °C on average), resulting in a persistently positive UHI index up to 3°C. Notably, a positive UHI index persists throughout the entire day, peaking in the evening before gradually decreasing overnight and reaching its minimum in the early morning. This diurnal cycle reflects the thermal properties of urban surfaces, whose higher heat capacity and lower albedo enhance daytime heat storage and slow night-time cooling (Kim and Brown, 2021). With the onset of the hot weather period (HW, which also stands for heatwave here) highlighted in yellow (21–26 August), temperatures rise substantially. Urban daily maxima reach nearly 39°C, while rural peaks stay closer to 36°C. The UHI intensity strengthens during this event, particularly between 22 and 24 August, with peak differences approaching 3.5 °C. This is consistent with findings in the literature, which indicate that typical characteristics of heatwave periods can amplify the thermal difference between urban and rural areas (Jiang et al., 2019). The intensification of the UHI during the HW arises from enhanced heat storage in urban materials and their lower albedo, which increase daytime energy absorption and delay nocturnal cooling. Reduced evaporative capacity of built-up surfaces further limits cooling efficiency, sustaining a stronger and more persistent UHI. As the HW ends and background temperatures decrease, these processes weaken and the UHI gradually declines, although residual heat remains due to the slow release of stored energy (Li and Bou-Zeid, 2013; Founda and Santamouris, 2017; An et al., 2020; Kim and Brown, 2021). After the heatwave (27 August), as background temperatures decrease, both T_U and T_R considerably reduce, and the UHI index shows a less pronounced diurnal cycle, reflecting the resumption of nocturnal radiative cooling, yet it remains positive due to residual heat stored in urban surfaces. This suggests that the reduction of T_{2m} influences urban areas more slowly than rural ones, highlighting the key role of thermal inertia of urban materials in prolonging extreme temperature conditions (Cai and Du, 2009; Berwal et al., 2016).

Fig. 6b shows the vertical cross-section of air temperature over the urban area of Bologna (44.4–44.6°N, 11.2–11.45°E) from 16 to 30 August 2023. A distinct diurnal cycle is evident in the lower troposphere, with daytime warming typically confined below ~ 800 m and near-surface (≤ 100 m) temperatures (defined as T_s) peaking around 14:00 UTC (16:00 local time). Before the onset of the HW, maximum T_s remains below 32 °C and nocturnal cooling leads to near-surface minima below 24 °C. Starting on 21 August, the onset of the HW marks a pronounced and sustained warming of the atmospheric column. Between 23 and 25 August, daily maximum T_s exceeds 37 °C, locally reaching ~ 41 °C, while the 30 °C isotherm progressively extends upward, peaking around 1500 m during early afternoon hours (14:00 UTC). The night-time temperatures remain high, often above 27 °C near the surface, with a notable suppression of nocturnal cooling below ~ 500 m. These conditions reflect an enhanced synergy between HW and UHI effects, characterized by persistent heat retention within the urban canopy layer. This synergistic intensification is likely driven by a combination of increased net radiation under clear-sky conditions, reduced evaporative cooling due to limited vegetation, atmospheric stability limiting advective cooling, and anthropogenic heat emissions (An et al., 2020; Zhao et al., 2018). Following the HW peak, a sharp thermal breakdown occurs after 27 August, with both surface and tropospheric temperatures declining significantly and the 30 °C isotherm no longer exceeding ~ 300 m.

Fig. 7 shows the horizontal thermal distribution by displaying the T_{2m} over the city of Bologna 2 days before HW event (hereafter defined as pre-HW day) and the day corresponding to maximum T_U according to Fig. 6a (hereafter defined max-HW day), namely 19 and 25 August 2023, respectively.

Fig. 7a shows the early morning spatial pattern of T_{2m} and over Bologna for pre-HW day during August 2023 event. The central region of the plot delimited by the red contour, corresponding to the urban city of Bologna, exhibits warmer temperatures with values between 24 °C and 27 °C during the early morning (05:00 UTC, approximately 07:00 local time, shortly after the 06:30 local sunrise). This is indicative of the UHI effect, where the densely built-up area (highlighted in the figures by a red contour line) has a higher thermal inertia that leads to elevated night-time temperatures compared to the surrounding rural areas. The surrounding region, especially toward the north and east, exhibits significantly lower temperatures during the night, highlighting how rural areas cool more efficiently due to the absence of heat-retaining infrastructure such as buildings and asphalt. Also, the northwestern rural areas exhibit a relatively uniform temperature distribution, which is consistent with open landscapes such as agricultural fields that tend to cool more during the night. In contrast, the warmer near-surface temperatures observed along the southern foothills of the Apennines (see Fig. 3c), compared to the cooler northern rural plains, can be attributed to several topographically driven processes. In the early morning, the southern hills receive direct solar radiation sooner due to their orientation, leading to earlier surface warming. Additionally, these elevated areas typically have drier soils, which heat more efficiently, and less effective nocturnal radiative cooling due to their exposure and slope geometry. Meanwhile, the northern plains, being relatively flat and enclosed, may experience cold air pooling overnight due to gravitational drainage from surrounding higher terrain, further enhancing the temperature contrast (Whiteman, 2000). Fig. 7b shows the early morning spatial pattern of T_{2m} and over Bologna for max-HW day during August 2023 event. An increase in T_{2m} across the entire domain is observable, with values in the range between 24–27 °C,

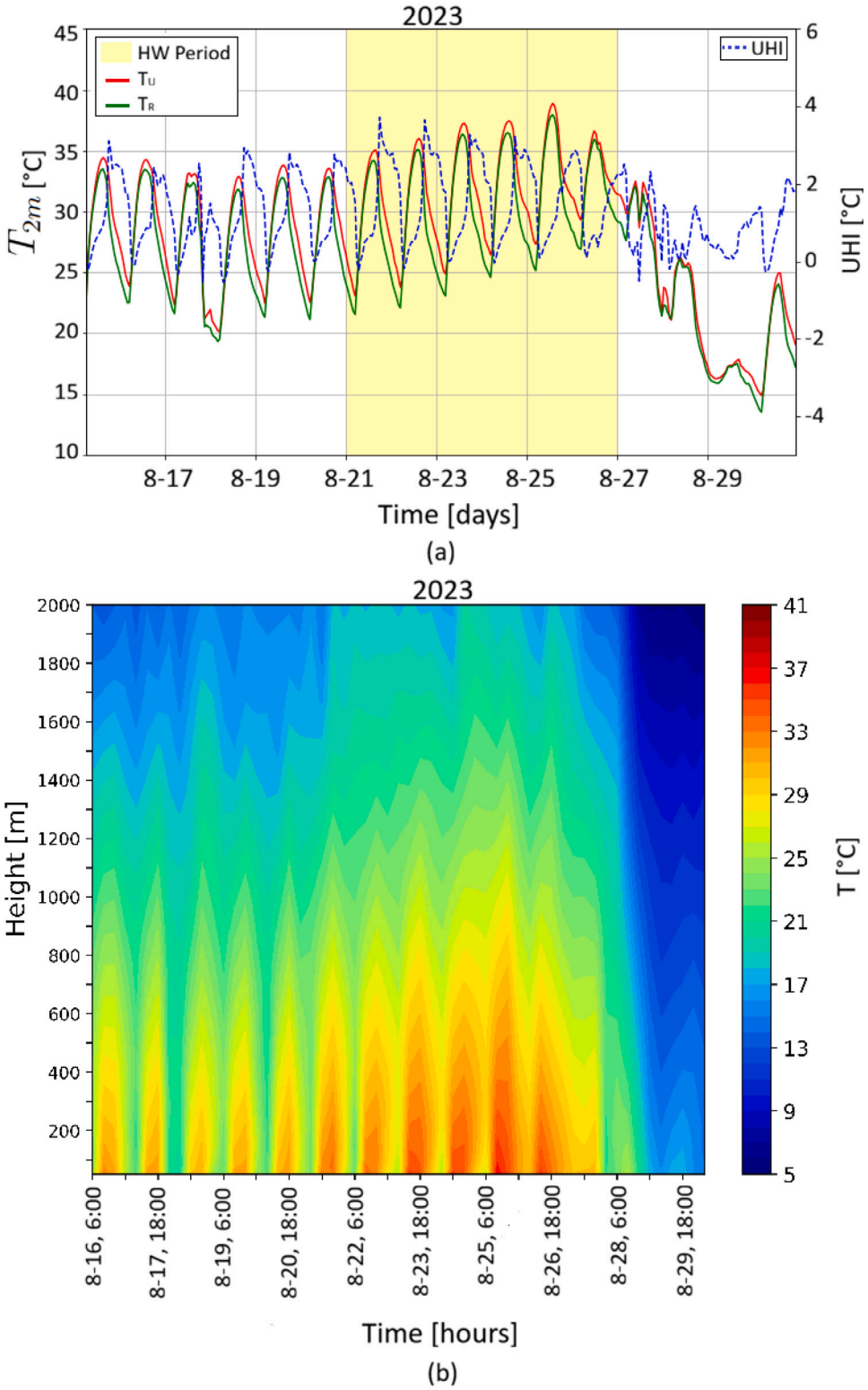

Fig. 6. *(a)* Timeseries of T_{2m} over Bologna during August 2023 heatwave: red line is the spatially averaged urban T_{2m} (T_U), green line is spatially averaged rural T_{2m} (T_R), and the blue line represents the UHI index. *(b)* Temporal evolution of time–height cross section of temperature over the urban area of Bologna during the August 2023 heatwave.

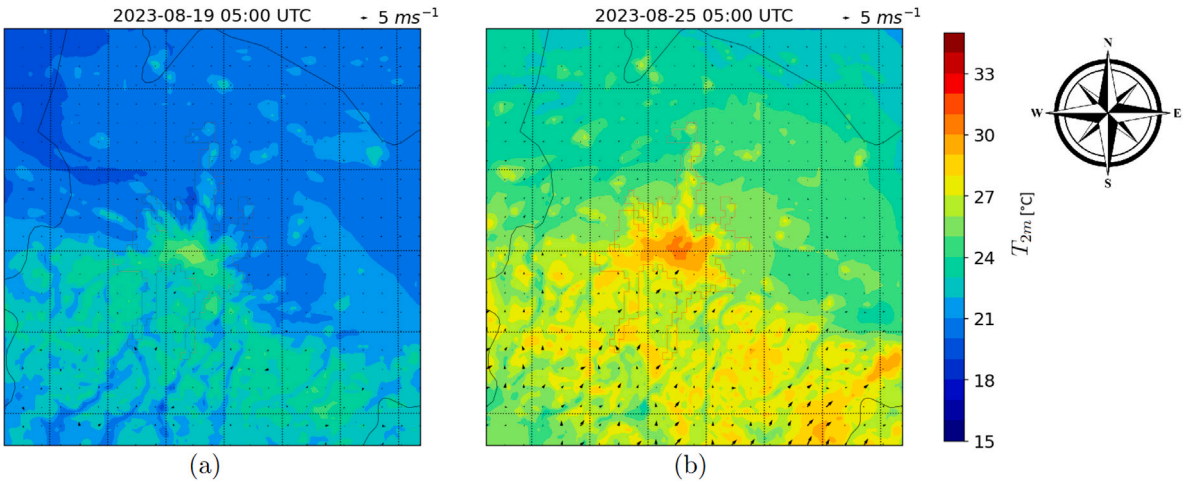

Fig. 7. Early morning spatial distribution of T_{2m} (temperature at 2 m from the ground) over Bologna for pre-HW *(a)* and max-HW *(b)* day regarding REF. Panels are representative of the hours when daily minimum temperature values are reached. The arrows represent the 10 m wind speed and direction w_{10m}. The red contour represents the border of the Bologna urban area based on Natural Earth data from MODIS (Justice et al., 2002).

confirming the persistence of elevated night-time and early morning temperatures during the heatwave event. As expected, the city center shows higher temperature values (Qiao et al., 2024; Sarangi et al., 2021), showing a distinct hot spot with temperatures exceeding 27 °C, whereas the pre-HW plot shows much lower temperature gradient between the city and its surroundings, with a weaker UHI index (< 3° C) compared to the HW plot (≥ 3° C). The weak near surface winds contribute to poor ventilation, especially in urban areas where buildings limit airflow (Theeuwes et al., 2017). Moreover, during the heatwave the pre-existing topographic effects are further amplified. The higher temperatures observed over the southern foothills of the Apennines compared to the pre-HW (Fig. 7a) indicate that during the heatwave these elevated areas undergo slower nocturnal cooling. Several physical processes may contribute to this behavior. First, persistent warm air advection at mid-levels can maintain elevated temperatures even over higher terrain (Geiger et al., 2009). Second, the reduced efficiency of radiative cooling at night (often associated with stable atmospheric stratification in elevated areas) can limit the loss of surface heat after sunset (Barry and Chorley, 2009). Finally, during the daytime, turbulent mixing and local downslope flows may transport warm air from higher altitudes downward, leading to heat accumulation near the surface, which is then retained during the night due to limited ventilation and thermal inertia. These mechanisms jointly result in a thermal contrast between the foothills and adjacent lowlands, where cooling is generally more efficient.

Fig. 8 illustrates the vertical profiles of temperature T and potential temperature $\theta = T\left(\frac{p_0}{p}\right)^{\kappa}$ (where p is atmospheric pressure, p_0 is the 1000 hPa reference pressure, and $\kappa = \frac{R}{c_p} \approx 0.286$) in the evening (20:00 UTC, approximately 22:00 local time, about 2 h after the 20:00 local sunset) at Bologna Idrografico (urban) and Mezzolara (rural) weather stations (see Fig. 3b).

Fig. 8a shows the vertical profiles of temperature T and potential temperature θ before the HW event. Near the surface (below ~ 20 m), the urban site exhibits T up to 2–3° C higher than the rural site, indicating a moderate UHI effect. This thermal contrast progressively decreases with height and becomes negligible above ~ 250 m, suggesting that the UHI effect is primarily confined to the lower atmospheric layers. The θ profiles reveal contrasting stability conditions between the urban and rural sites. After the first 50 m, urban potential temperature θ_U remains nearly constant with height, indicating a neutrally stratified layer. This suggests that mechanical turbulence, enhanced by the urban canopy, supports vertical mixing and prevents the development of thermally stable stratified boundary layer. In contrast, the rural profile exhibits an increase in potential temperature θ_R, with a vertical gradient of ~ 2° C/100 m, indicative of thermal stable stratification. This feature is consistent with radiative cooling of rural surfaces after sunset, which leads to the formation of a near-surface temperature inversion and reduced vertical mixing (Fernando, 2010). Fig. 8b shows the vertical profiles of temperature T and potential temperature θ during the HW event. Compared to the pre-HW case, the overall T is significantly higher in both locations, reaching values near 35 °C at the surface in the urban area. The urban–rural temperature difference near the surface exceeds 2 °C and remains pronounced up to approximately 200 m altitude, indicating a stronger and more vertically confined UHI effect under HW conditions. Regarding θ profiles, it is notable that the onset of the HW intensifies both radiative cooling over rural areas and heat release from urban surfaces. This dual mechanism sharpens the contrast in low-level stratification (the lowest 50 m): increasing stability over rural areas (exacerbated $\frac{d\theta_U}{dz} > 0$) and promoting temporary instability in urban environments (enhanced $\frac{d\theta_R}{dz} < 0$). Overall, the increased thermal contrast and vertical stability difference between the two environments contributes to an intensification of the UHI effect during the HW event.

3.2. Horizontal thermal pattern under future scenarios

This section examines the behavior of T_{2m} under future climate scenarios, focusing on both the temporal evolution and the horizontal spatial distribution at specific times.

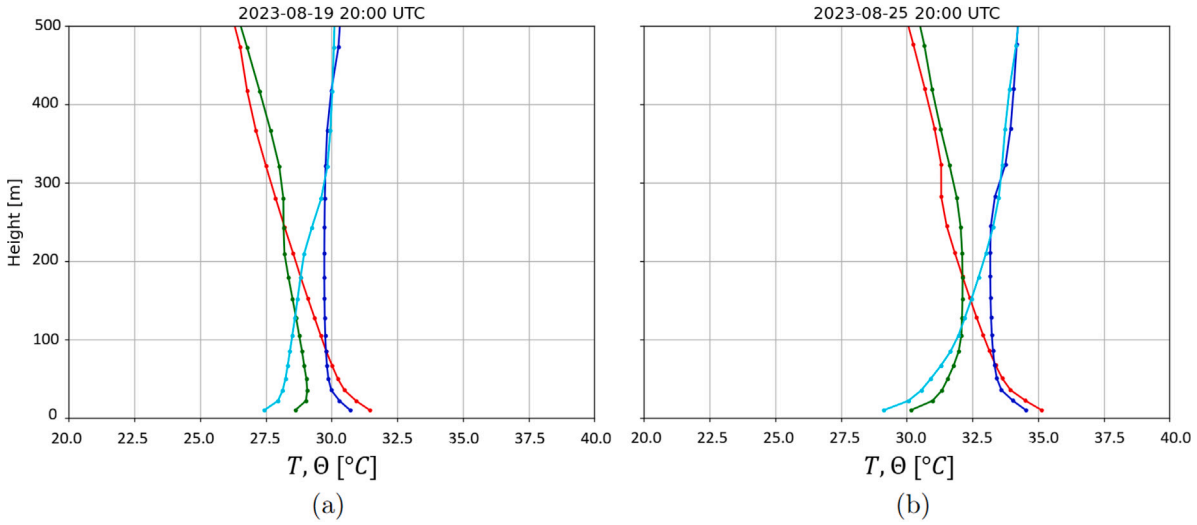

Fig. 8. Evening vertical profile of T and potential temperature θ for urban Bologna Idrografico and rural Mezzolara locations for pre-HW *(a)* and max-HW *(b)*, namely 19 and 25 August 2023. Red and green lines represent the temperature profiles at the urban and rural locations, respectively, while blue and cyan lines show the corresponding potential temperature profiles.

3.2.1. *Temporal evolution of T_{2m}*

Fig. 9 shows the T_{2m} profiles in urban areas during HW events (marked by yellow shading) for the 4 different cases listed in Table 2, alongside the urban–rural thermal difference represented by the UHI index.

Fig. 9a reports the 4 days NF-585 event. Here, T_U exceeds T_R throughout the study period at night, with nocturnal UHI index values frequently surpassing 3 °C, also increasing and peaking at 5 °C during HW nights. Daytime T_U and T_R notably increase during HW days, peaking above 40 °C, but they reveal an inappreciable difference, which in some occasions leads to UHI index ≤ 0. The amplitude of the urban diurnal cycle is reduced compared to the rural curve, with urban areas exhibiting limited night-time cooling. Fig. 9b describes the 5 days NF-245 event, in which daytime T_U and T_R reach similar values compared to NF-585 event, with maxima above 40 °C. Also in this case, despite rural areas experiencing similarly high daytime temperatures, especially during HW nocturnal cooling is more efficient outside the urban area: night-time T_R drops below 24-25 °C, whereas T_U remains higher. This results in a persistent night-time UHI intensity of approximately 4.5 °C. Particularly near the end of the HW event (26–27 August), the steep rise in T_R temporarily reduces the UHI index, which becomes even slightly negative. Fig. 6c shows the FF-585 case, which features the most prolonged HW (10 days) among the examined events. This case is characterized by persistent but not extremely high temperatures, with T_U and T_R daily maxima rarely exceeding 34 °C. Despite the absence of extreme daytime peaks, the HW period shows an almost constant difference in nocturnal T_U and T_R, producing a sustained UHI effect. The UHI index increases significantly during the HW period, remaining mostly between 3–4 °C. Also in this case, the UHI index occasionally turns negative. Fig. 6d illustrates the 5 days FF-245 event. Daily maxima of both T_U and T_R generally remain below 35 °C, except for the HW days. UHI intensity during this case is slightly lower than in the other scenarios, typically remaining slightly above 3 °C during the HW period. Although both T_U and T_R rise during the HW, the UHI index shows only a limited increase, suggesting a more parallel evolution of urban and rural temperatures during extreme conditions. A particularly noteworthy aspect is that the highest UHI values are recorded after the end of the HW period, despite a general cooling in both urban and rural temperatures. All five cases — including the reference year 2023 (REF) — show a clear UHI effect, yet with notable differences in terms of intensity, temporal dynamics, and response to HW events. The REF case exhibits a moderate but consistent UHI, with average intensity around 0.5 °C and peaks reaching ~ 3.5° C during the HW period. Importantly, the UHI index in REF remains negligible or positive throughout the day, with a well-defined diurnal cycle. The two near-future events (NF-585 and NF-245) are characterized by extremely high daytime temperatures, with both T_U and T_R exceeding 40 °C, particularly during HW peaks. However, the UHI intensity during the day tends to diminish, occasionally dropping to zero or becoming negative due to the parallel rise in rural temperatures, more than in REF case. Nocturnal UHI, on the other hand, is more persistent and intense, frequently exceeding 4 °C, especially in NF-585 where it peaks around 5 °C during HW nights. The far-future cases (FF-585 and FF-245) exhibit less extreme absolute temperatures: daily maxima of T_U and T_R mostly remain below 35 °C. Nevertheless, these events show a sustained nocturnal UHI effect, indicating that persistent thermal stress in urban areas can occur even in the absence of extremely high temperature peaks. In the prolonged FF-585 event, the UHI index remains steadily between 3–4 °C during HW nights, while in FF-245 the UHI intensity is slightly weaker and less responsive to the HW itself, maintaining values just above 3 °C, but the highest UHI values emerge after the end of the HW, despite an overall cooling trend in both T_U and T_R. This behavior diverges from the REF case, where the UHI peaks during the HW

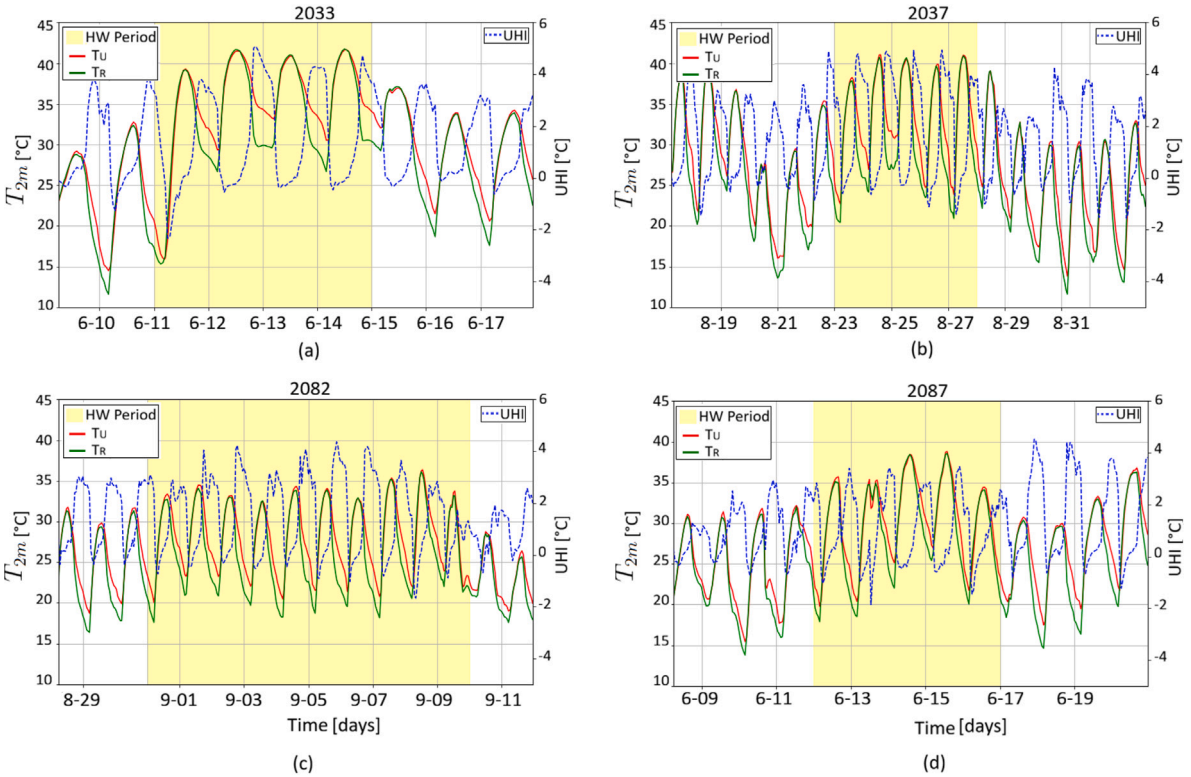

Fig. 9. Timeseries of T_{2m} over Bologna: red line is the spatially averaged urban T_{2m} (T_U), green line is spatially averaged rural T_{2m} (T_R), and the blue line represents the evolution of UHI index. Panels refer to the 4 selected "hot weather" events: NF-585 *(a)*, NF-245 *(b)*, FF-585 *(c)* and FF-245 *(d)*.

Table 3
Average of daily peak values of T_U and T_R (daytime) and peak UHI (night-time) for each case and period (Pre_{HW}, HW, Post_{HW}).

Label	T_U			T_R			UHI		
	Pre_{HW}	HW	Post_{HW}	Pre_{HW}	HW	Post_{HW}	Pre_{HW}	HW	Post_{HW}
NF-585	31.2	40.5	35.1	29.3	39.5	33.4	3.5	4.0	3.1
NF-245	36.0	39.5	33.6	34.5	39.5	32.7	3.5	4.5	3.3
FF-585	32.3	34.5	30.5	29.7	31.6	27.4	3.5	4.5	3.1
FF-245	32.3	36.5	31.5	30.6	34.5	29.4	3.5	4.5	3.0
REF	34.5	38.4	33.4	32.6	35.8	31.3	3.1	4.0	3.2

and weakens after it, highlighting a temporal shift in UHI dynamics. To quantitatively support these observations, average daily peak values of urban temperature (T_U) and rural temperature (T_R), together with peak night-time UHI, were computed for the five analyzed cases (NF-585, NF-245, FF-585, FF-245 and REF), distinguishing three key periods: before the event (Pre_{HW}), during the event (HW), and after the event (Post_{HW}) (see Table 3).

Table 3 confirms the main contrasts among scenarios. Near-future cases (NF-585 and NF-245) record the highest daytime urban temperatures during HW, peaking at 40.5 °C and 39.5 °C, respectively, while rural temperatures rise in parallel, reducing daytime UHI differences. Despite this, night-time UHI remains strong, averaging 4.0–4.5 °C during HW. Far-future scenarios (FF-585 and FF-245) show lower absolute temperatures (urban peaks of 34.5–36.5 °C), yet maintain similar nocturnal UHI values (4.5 °C) and exhibit persistence after HW, indicating urban thermal inertia. The REF case lies in between, with HW peaks of 38.5 °C and UHI around 4.0 °C.

In general, while near-future scenarios are marked by short and intense HW events with stronger fluctuations in UHI, far-future scenarios — especially under lower emissions (FF-585) — highlight the risk of chronic nocturnal urban overheating, even in the absence of extreme daytime heat. The comparative analysis suggests that UHI dynamics are governed not only by absolute temperatures, but also by the interplay between rural and urban thermal inertia, which evolves differently across emission pathways and future periods. While the REF case displays a predictable diurnal UHI pattern that intensifies during HWs but quickly relaxes afterward, future conditions — especially under high-emission or prolonged HW scenarios — are likely to induce more persistent nocturnal overheating, regardless of the presence of extreme temperature peaks.

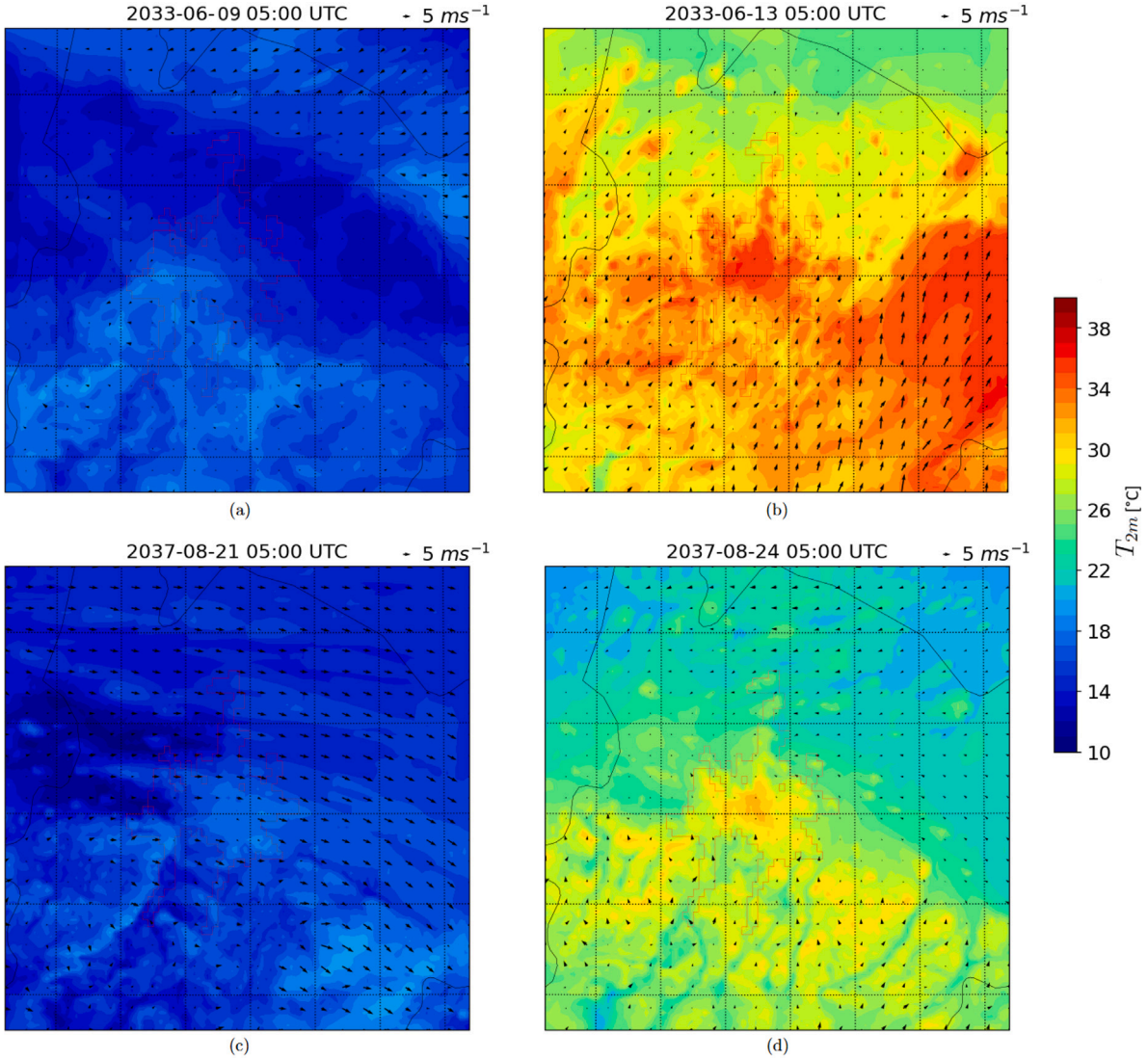

Fig. 10. Early morning spatial distribution of T_{2m} over Bologna for pre-HW *(a)* and max-HW *(b)* day regarding NF-585, and for pre-HW *(c)* and max-HW *(d)* day regarding NF-245. The arrows represent the 10 m wind speed and direction. The red contour represents the border of the Bologna urban area based on Natural Earth data from MODIS.

3.2.2. Horizontal spatial distribution of T_{2m}

The analysis of the spatial patterns of T_{2m} over Bologna reveals distinct trends in UHI intensity across different years and SSP scenarios. As previously done for the REF case, Fig. 10 illustrates these patterns for NF-585 and NF-245 cases 2 days before the HW event (pre-HW) and during the day corresponding to maximum T_U (max-HW) according to the respective panels in Fig. 9. Panels are representative of the hours when daily minimum temperature values are reached, namely at 05:00 UTC (07:00 local time), shortly after the 06:30 sunrise.

Fig. 10a shows the pre-HW conditions for NF-585. The T_{2m} field is relatively uniform (12–18° C), and no significant urban UHI effect is evident at this hour, since the urban area does not stand out thermally from the surrounding rural landscape. Fig. 10b shows the max-HW day for NF-585, where T_{2m} rise significantly throughout the domain (> 30° C). Urban areas undergo a significant warming, but an exacerbation of UHI effect is not observable, as similar temperatures are observed in the surrounding peri-urban (land cover classes 55–56 in Fig. 4) and rural areas. Fig. 10c shows the pre-HW day under the NF-245 scenario, with T_{2m} ranging between 12-20 °C. Slightly warmer conditions are observed within the urban area, particularly when compared to the northern and western rural surroundings, suggesting the presence of a moderate UHI effect (UHI index ~ 1° C). Fig. 10d shows the max-HW day for NF-245, where temperatures generally ranging from 22 °C to 28 °C across the region. The urban area exhibits high T_{2m} with respect to the surrounding rural region, particularly to the north and north-east. This indicates a UHI effect, with the strongest contrast in the zones of dense urban development (land cover classes 52–53 in Fig. 4). In contrast, high T_{2m} values in the southern

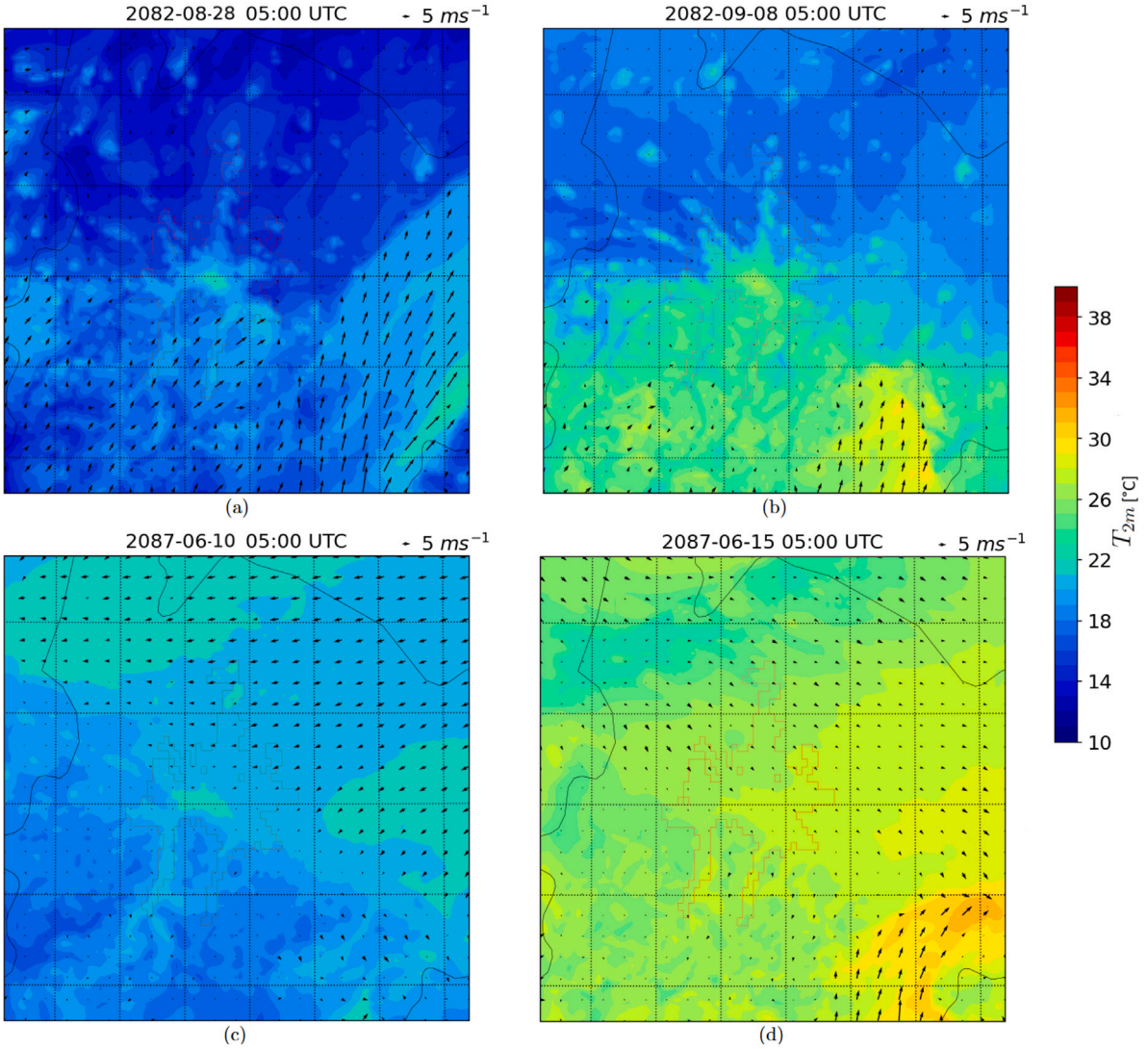

Fig. 11. Early morning spatial distribution of T_{2m} over Bologna for pre-HW *(a)* and max-HW *(b)* day regarding FF-585, and for pre-HW *(c)* and max-HW *(d)* day regarding FF-245. The arrows represent the 10 m wind speed and direction. The red contour represents the border of the Bologna urban area based on Natural Earth data from MODIS.

region appear unrelated to urban land cover, and are influenced by other meteorological factors as discussed for the REF case (see Fig. 7b).

Fig. 11 illustrates T_{2m} patterns for FF-585 and FF-245 cases 2 days before the HW event (pre-HW) and during the day corresponding to maximum T_U (max-HW) according to respective panels in Fig. 9. Also in these cases, panels are representative of the hours when daily minimum temperature values are reached, namely at 05:00 UTC (07:00 local time), shortly after the 06:30 sunrise.

Fig. 11a shows the pre-HW day for FF-585. The T_{2m} field is not uniform (14–24° C), and higher values are observed in the urban areas of Bologna compared to the rural surroundings. This suggests the onset of a moderate UHI effect (UHI index ∼ 2° C) even before the HW event. Fig. 11b shows the max-HW day for FF-585. The urban area exhibits notably higher temperatures than its northern surroundings, with the city center exceeding 28 °C, leading to a strong UHI index (∼ 4° C). The Apennines side increase in T_{2m} is similar to that observed in the REF (Fig. 7b) and NF-245 (Fig. 10d) cases. Fig. 11c shows the pre-HW day for FF-245. The T_{2m} distribution reveals limited contrast between urban and rural areas, therefore the UHI effect is almost negligible. Fig. 11d shows the max-HW day for FF-245. T_{2m} rises across the domain but remain lower than in the FF-585 scenario. The temperature increase is uniform across the domain, regardless of whether the area is urban or rural, so the UHI effect is negligible.

A comparative analysis across present, near future, and far future scenarios reveals notable differences in T_{2m} intensity and spatial pattern under varying emission pathways, also concerning the UHI effect. In the REF case, the UHI is already evident before

the HW, with early morning urban temperatures exceeding those in the rural surroundings due to thermal inertia. This contrast strengthens during the HW, with a clear urban hotspot and persistent high temperatures. In the near future, differences between the two scenarios emerge more clearly during the HW event. In NF-585, no UHI effect is observed before the HW, and even during the HW, despite a general temperature rise across the domain, the UHI signal remains weak due to relatively homogeneous warming. In contrast, NF-245 already shows a moderate UHI before the HW, which becomes more evident during the HW, especially over dense urban zones. This highlights the greater spatial contrast in SSP245 compared to SSP585, despite the lower overall warming. In the far future, the divergence between the scenarios is even more pronounced. In FF-585, a strong UHI effect is present already before the HW, and it becomes significantly amplified during the HW, with urban–rural temperature differences up to ~ 4° C. This points to a more persistent and intense UHI effect under high-emissions scenarios. On the other hand, in FF-245, the temperature distribution remains nearly uniform both before and during the HW, with no notable UHI signal, suggesting that emission mitigation strongly limits future UHI intensification. The increasingly evident differences between SSPs in the far future are consistent with global projections (Hajat et al., 2023; Norgate et al., 2024) and IPCC assessments (Shukla et al., 2022), which highlight that scenario-driven temperature contrasts become more significant over time as greenhouse gas emissions diverge.

3.3. Vertical thermal structure under future scenarios

This section examines the vertical distribution of temperature under future climate scenarios, focusing on both the temporal evolution of the thermal structure and the vertical profiles at specific times.

3.3.1. Time–height cross section of temperature

Fig. 12 shows the temporal evolution of time–height cross sections of temperature (in °C) over the urban area of Bologna (44.4–44.6°N, 11.2–11.45°E) for NF-585, NF-245, FF-585 and FF-245 cases. The vertical axis spans from the surface up to 2000 m above sea level, and time is given in UTC.

Fig. 12a shows the NF-585 case. The HW event (11–16 June) is characterized by a strong increase in near-surface (below 100 m) temperature T_s compared to pre-HW days, and it reaches 41 °C during the central days of the event. The 30 °C isotherm rises up to 1100 m during the HW period, indicating a deep and well-developed mixed layer. This vertical extension of warm air reduces static stability and can initially favor vertical mixing and pollutant dispersion. However, the intense and persistent heating also leads to a strong capping inversion above the mixed layer, which may later inhibit vertical exchange and favor pollutant accumulation near the surface, particularly during the evening and night hours. During HW period, nocturnal cooling is significantly suppressed: even during early morning hours (04:00–06:00 UTC) T_s remains above 30 °C, indicating strong heat retention. Night-time temperatures remain elevated, particularly below 200 m where values stay above 27 °C throughout the night. A high vertical temperature gradient (> 1 °C/100 m) persists below 1000 m, indicating partial stratification. After the HW ends, a distinct diurnal cycle resumes, though both daytime maxima and night-time minima remain slightly higher compared to pre-HW conditions. Fig. 12b shows the NF-245. The HW event (23–28 August) is characterized by a pronounced increase in T_s with respect to pre-HW days, surpassing 40 °C. The 30 °C isotherm rises up to 1000 m, though not as high as in NF-585. During the HW peak, nocturnal cooling is significantly reduced: even at 06:00 UTC, T_s stays around 30 °C. This persistent night-time heat suggests an urban heat retention effect, though less pronounced than in NF-585. The moderate vertical temperature gradient present below 500 m (~ 1 °C/100 m) indicates limited vertical mixing. Following the HW, a distinct diurnal cycle resumes, as T_s ranges from 18 °C at night to 28 °C during the day, which are slightly reduced values with respect to pre-HW conditions. Fig. 12c shows the FF-585 case. A prolonged 10-day HW event is observed (30 August-10 September). Even before the HW onset, daytime T_s peaks around 30 °C, with nocturnal cooling allowing to drop to 23 °C. The HW event is marked by warming throughout the atmospheric column, and T_s exceed 33 °C during the central hours of the day. The 30 °C isotherm is confined below 200–300 m throughout the first HW days, then extends up to 500 m near the HW end. The vertical temperature gradient becomes notably small throughout the first 1000 m (< 0.5 °C/100 m), which reveals a weak stratification and a highly mixed layer. Following the HW, a diurnal cycle resumes, with both day and night temperatures lower compared to pre-HW values. Fig. 12d shows the FF-245 case. Compared to pre-HW days, the HW period (12–16 June) is characterized by an increase in T_s, which peaks at 38 °C. It is possible to observe a gradual increase of temperature simultaneously to the HW development, and the 30 °C isotherm rises to a maximum altitude of 800 m during the central HW days (14–15 June). A moderate vertical gradient (~ 1 °C/100 m) is notable in the first 800 m, indicating partial stratification and mixing efficiency. After the HW event, a regular diurnal cycle re-establishes, with daytime maxima and night-time minima similar to pre-HW conditions.

A comparison across the five cases (NF-585, NF-245, FF-585, FF-245 and REF described in Section 3.1.2) reveals both common thermal responses to HW events and distinct features tied to scenario and period. In all cases, HW periods are characterized by intensified near-surface warming, upward displacement of the 30 °C isotherm, and reduced nocturnal cooling, signaling enhanced heat retention. The NF-585 and NF-245 scenarios exhibit similar thermal patterns, but the NF-585 case shows stronger heat accumulation and suppressed nocturnal cooling, suggesting more intense effect of urban warming compared to NF-245. In the far future scenarios, FF-585 displays a prolonged HW period with a markedly weak vertical temperature gradient, indicating a highly mixed and weakly stratified lower troposphere, unlike FF-245, which maintains a more defined vertical gradient and limited warming confined below 800 m. While all future scenarios show HW amplification relative to REF, the intensity, persistence, and vertical extent vary across SSPs and time horizons. These differences in vertical temperature structure have important implications for atmospheric stability and pollutant dispersion: the weakened stratification and deeper mixed layers observed in SSP585 scenarios favor turbulent mixing and vertical transport during daytime, but can also enhance the accumulation of pollutants near the surface under nocturnal inversions. Overall, SSP585 scenarios (both near and far future) are associated with more pronounced thermal stress, reduced cooling capacity, and signals of stronger stratification breakdown compared to SSP245, highlighting the role of emission pathways in shaping future urban thermal extremes.

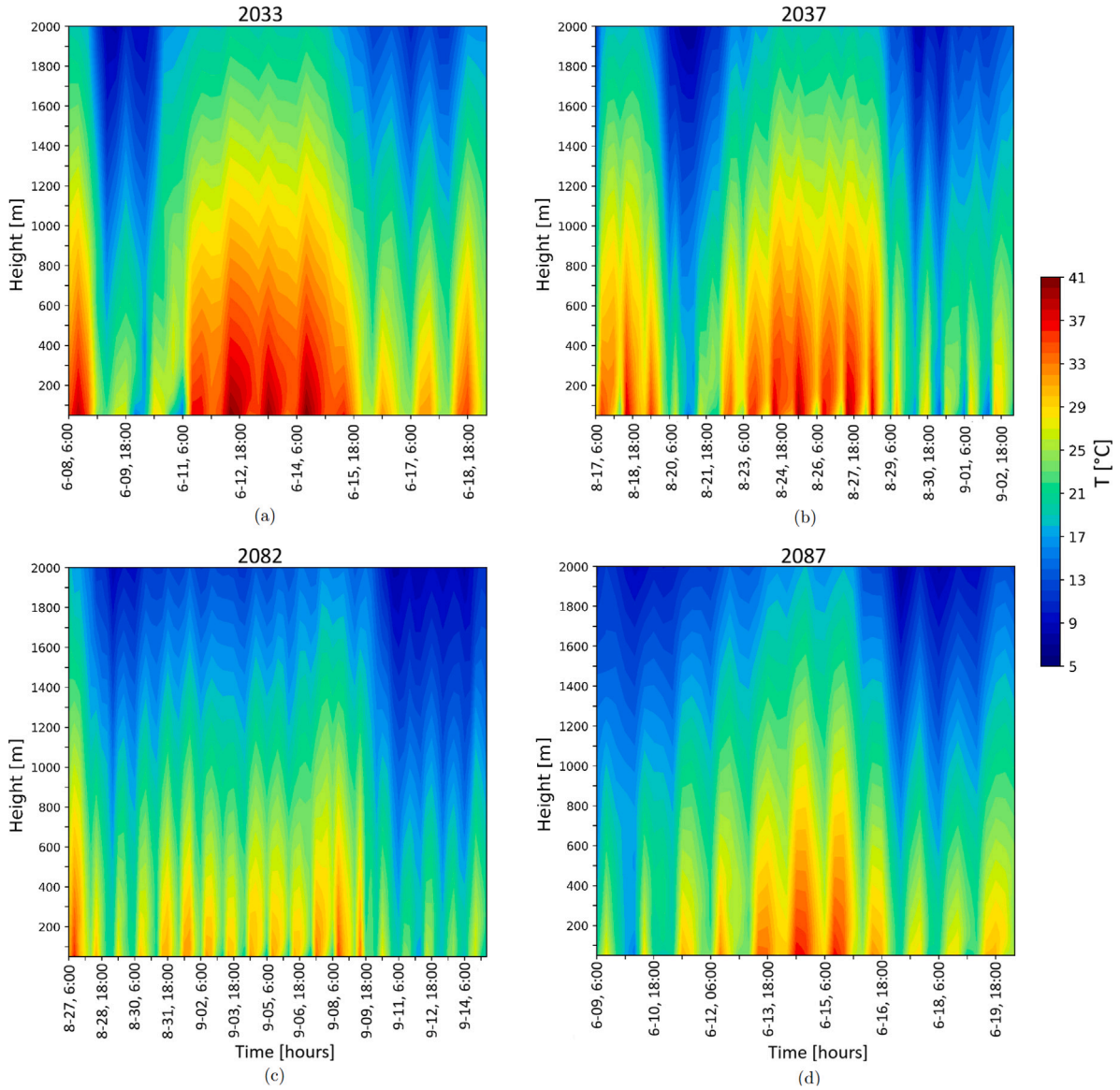

Fig. 12. Temporal evolution of time–height cross section of temperature over the urban area of Bologna for NF-585 *(a)*, NF-245 *(b)*, FF-585 *(c)* and FF-245 *(b)* HW events.

3.3.2. Thermal vertical profile

Fig. 13 illustrates the vertical profiles of temperature T and potential temperature θ in the evening (20:00 UTC) at Bologna Idrografico (urban) and Mezzolara (rural) weather stations for pre-HW and HW days for near-future cases NF-585 and NF-245.

Fig. 13a shows the pre-HW day for the NF-585 case. Close to the surface (below 20 m), the urban location exhibits slightly higher T (3–4 °C) than the rural site, suggesting a detectable positive UHI effect. Temperature differences between the two sites diminish with height, becoming negligible at ~ 140 m. The θ profiles reveal differences in atmospheric stability: at the urban site, θ remains relatively constant up to about 200 m, indicating a neutrally stratified layer. This behavior indicates enhanced turbulent mixing, due to the roughness of the urban surface and residual mechanical turbulence after sunset. In contrast, the rural θ profile shows a pronounced increase with height, with a gradient of ~ 2 °C/100 m, pointing to a stable stratification typical of nocturnal cooling over vegetated surfaces. Fig. 13b exhibits the max-HW day for the NF-585 case. Near-surface T are markedly high at both sites, with a ~ 10° C increase compared to the pre-HW situation. The urban–rural thermal contrast reveals similar to pre-HW in the first 20 m, but it diminishes rapidly with height and becomes negligible at 50 m, suggesting that the UHI is more vertically limited than in pre-HW conditions. The θ profiles show analogous characteristics to pre-HW, but the rural site shows a sharper increase with height. Fig. 13c shows the pre-HW day for the NF-245 case. Near the surface, the urban site displays T about 1.5 °C higher

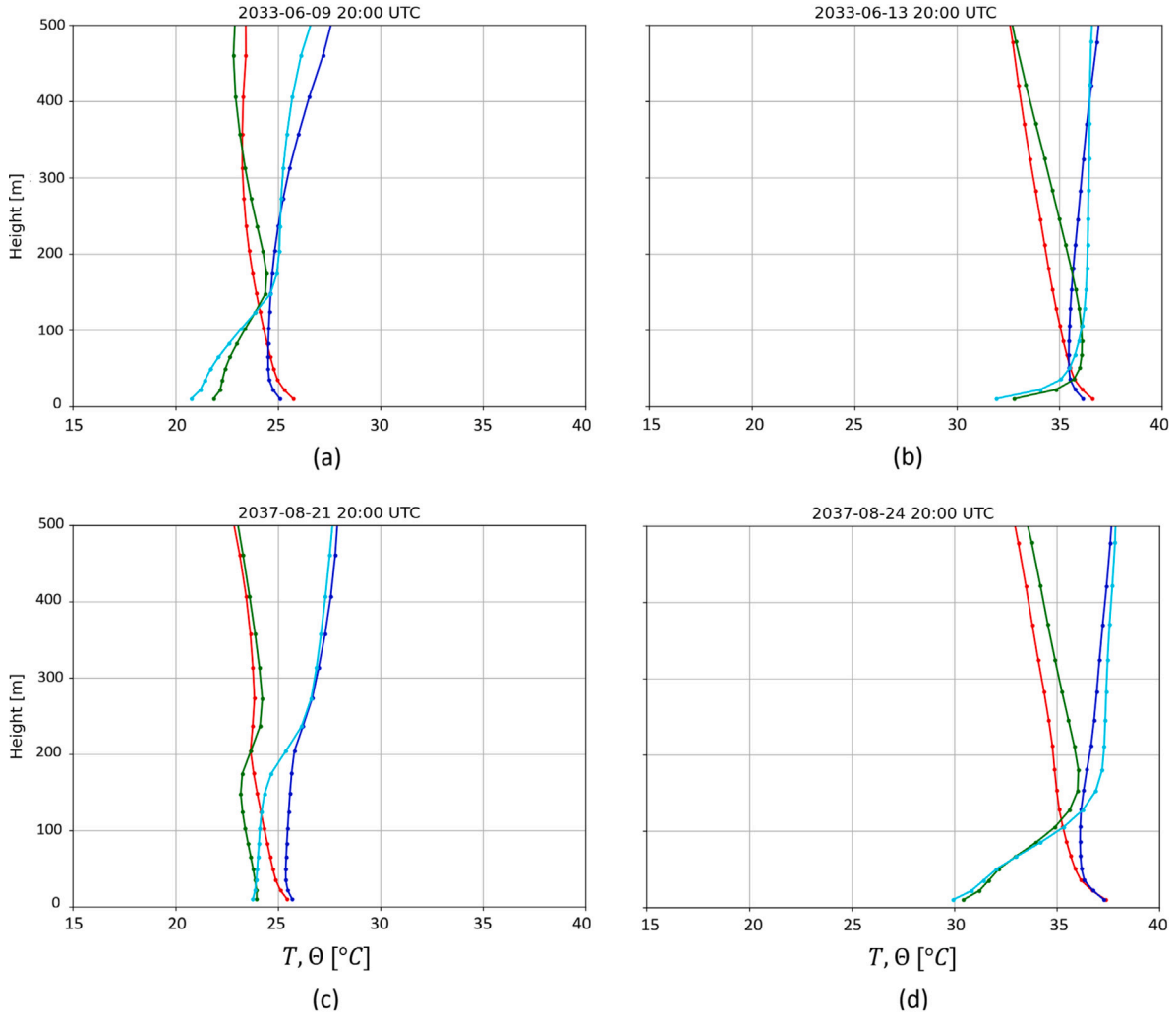

Fig. 13. Evening vertical profile of T and θ for urban Bologna Idrografico (red and blue) and rural Mezzolara (green and cyan) locations for pre-HW *(a)* and max-HW *(b)* days for case NF-585, and for pre-HW *(c)* and max-HW *(d)* days for case NF-245.

than the rural site, and this thermal contrast remains constant with height before becoming negligible above 200 m. The urban θ profile is relatively flat up to 200 m, suggesting near-neutral stratification, while the rural site exhibits an increase in θ with height with a small gradient(> 1 °C/100 m), consistent with the development of stable stratification. Fig. 12d shows the max-HW day for the NF-245 case. Near the surface, the urban location exhibits a T up to 7 °C higher than the rural, indicating a strong UHI effect. This temperature difference rapidly diminish with height, becomes negligible at ∼ 100 m, suggesting that the UHI is intensified but also more shallow compared to pre-HW conditions. The urban θ profile is relatively flat, connected to weakly stable conditions. Conversely, the rural profile shows a steep gradient in θ (5°C/100 m), typical of strongly stable stratification. Compared to the pre-HW case, the near-surface layer appears more stably stratified over the rural area, which leads to a vertically confined positive UHI during HW conditions.

Fig. 14 shows the vertical profiles of temperature T and potential temperature θ in the evening (20:00 UTC) at Bologna Idrografico (urban) and Mezzolara (rural) weather stations for pre-HW and HW days for far-future cases FF-585 and FF-245.

Fig. 14a shows the pre-HW day for the FF-585 case. Near the surface, the urban site is 5 °C warmer than the rural, then T difference gradually decreases with height and becomes negligible at ∼ 200 m, where the positive UHI is limited. Over the urban site, θ remains constant, while the rural profile shows an increasing θ with height at a rate of ∼ 1.5 °C/100 m for the first 200 m, signature of stable stratification. Fig. 14b shows the max-HW day for the FF-585 case. Compared to the pre-HW situation, the urban–rural T contrast near the surface is exacerbated, with differences of 7 °C, indicating a stronger UHI effect. This T difference sharply decreases with height up to ∼ 120 m, indicating that the positive UHI effect is enhanced in intensity but reduced in vertical depth compared to pre-HW conditions. The urban θ profile shows a nearly neutral layer, and the rural profile exhibits a more stable vertical gradient in the first 100 m, with θ increasing by about 5.5 °C/100 m. Fig. 14c shows pre-HW day for FF-245 case. This

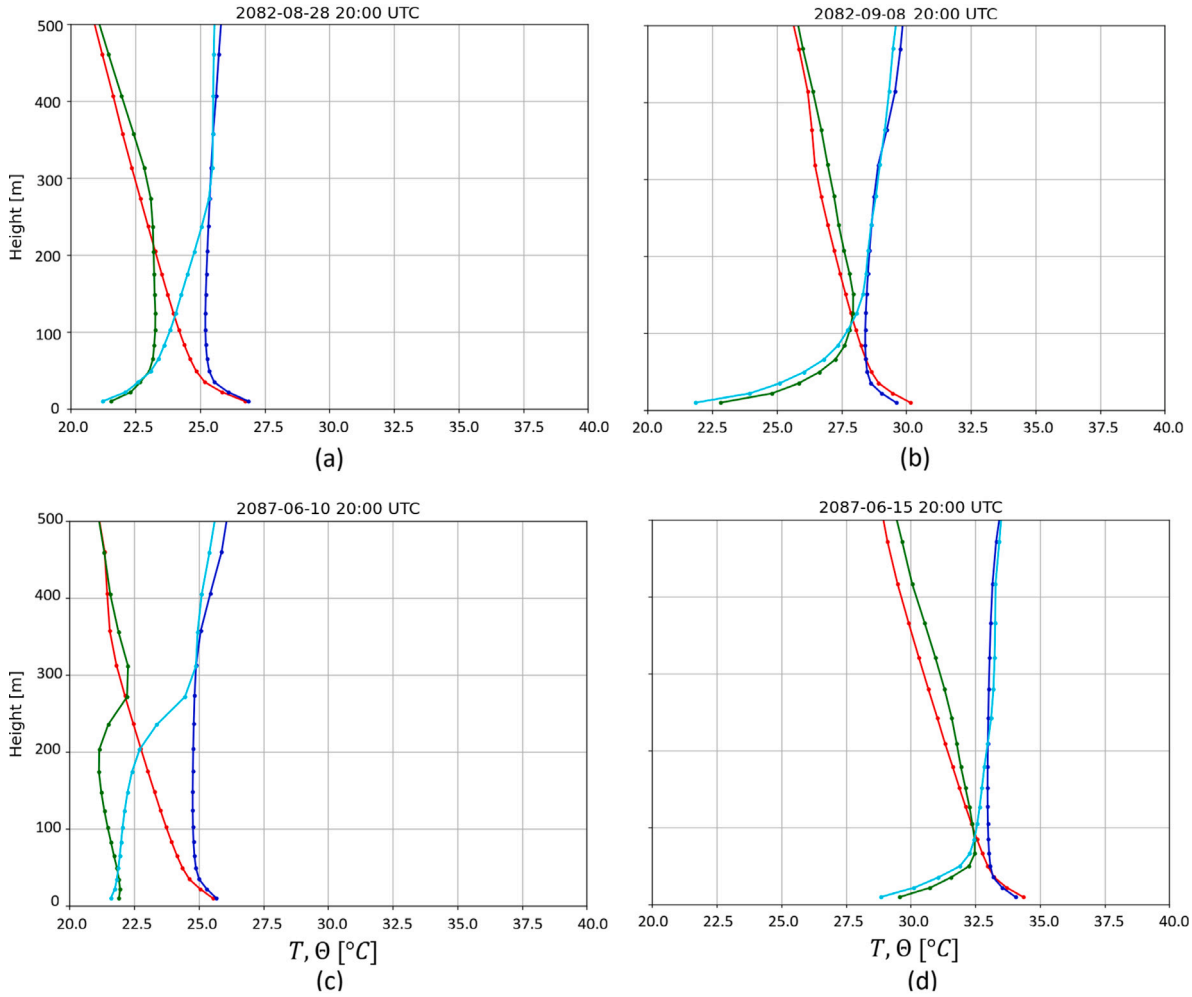

Fig. 14. Evening vertical profile of T and θ for urban Bologna Idrografico (red and blue) and rural Mezzolara (green and cyan) locations for pre-HW *(a)* and max-HW *(b)* days for case FF-585, and for pre-HW *(c)* and max-HW *(d)* days for case FF-245.

case exhibits relatively low T, with the urban area not exceeding 26 °C and the rural one impacted by about 22 °C, indicating a UHI intensity of about 3.5–4 °C which decrease up to ~ 270 m. Urban θ profile is constant throughout the column, while the rural profile shows a θ gradient (1°C/100 m) up to 300 m height, consistent with the onset of a stable layer. Fig. 14d shows the max-HW day for the FF-245 case. Surface temperatures are significantly higher than pre-HW, with the urban site reaching nearly 33 °C and the rural site about 30 °C, indicating an UHI intensity of approximately 3 °C and a vertical extension of 100 m. The urban θ profile appears constant with height, while the rural displays a sharp increase in the first 100 m, denoting the formation of a stable layer as the surface cools more efficiently. Compared to the pre-HW period, the thermal structure here reflects intensified urban–rural contrast, with a more pronounced and vertically confined UHI.

A comparison between the REF case (see Section 3.1.2) and future scenarios reveals consistent structural features of the thermal vertical profiles, along with notable variations in intensity and vertical extent across time horizons and emission pathways. In all cases, urban sites exhibit higher near-surface temperatures than rural sites, confirming a persistent positive UHI effect. However, its magnitude and vertical reach vary. Under REF conditions, the UHI reaches 2–3 °C near the surface and fades above ~ 250 m. In near-future scenarios, the UHI is generally more intense (up to 4 °C in NF-585 and 7 °C in NF-245 during HW events) but becomes vertically shallower, often confined below 100–140 m, indicating a more concentrated but limited UHI under warming scenarios. A similar pattern is observed in the far future: FF-585 shows peak differences of 7 °C during HW, yet the thermal contrast vanishes by ~ 120 m; FF-245, despite lower absolute temperatures, also displays a shallow but clear UHI (up to 3.5–4 °C), extending up to ~ 270 m pre-HW and reducing to less than 100 m during HW. Across all SSPs, urban θ profiles consistently suggest neutral or weakly stable stratification, indicating enhanced mechanical turbulence and efficient vertical mixing over built areas. In contrast, rural profiles generally exhibit increasing potential temperature with height, signaling stable nocturnal conditions intensified under HW events. These contrasting stability regimes have relevant implications for pollutant dispersion: urban areas, despite stronger heating,

may experience more efficient dilution of near-surface pollutants during daytime due to enhanced mixing, whereas rural zones — especially under stable night-time conditions — are more prone to pollutant accumulation and reduced ventilation. During HWs, the overall shallowing of the mixed layer in both environments can further limit dispersion and exacerbate air quality deterioration. Notably, the strongest stratification and shallowest UHI layers occur during HWs in both near and far future, pointing to a compound and synergistic effect of urban heating and rural cooling. Comparing SSPs, the 585 pathway consistently leads to higher surface temperatures and stronger UHI intensities near the surface compared to the 245 scenarios. However, the depth of the urban neutral stratification layer remains broadly similar across SSPs. Interestingly, rural areas in SSP245 cases sometimes exhibit steeper stability gradients, suggesting enhanced nocturnal stratification. Overall, while the urban–rural thermal contrast intensifies under future HW conditions (especially in SSP585) the vertical extent of the UHI becomes more confined, indicating a shift in its vertical structure under climate change.

3.4. Brief discussion on practical recommendations for mitigation and adaptation

The contrasting thermal behaviors identified across emission pathways provide useful guidance for climate adaptation strategies. Under the high-emission SSP585 scenario, prolonged nocturnal heat retention and suppressed night-time cooling suggest that mitigation should prioritize measures enhancing nocturnal ventilation and radiative heat loss—such as increased urban greenery, reflective materials, and ventilation corridors (Santamouris, 2014; Irfeey et al., 2023). These interventions are particularly relevant in dense urban fabrics where heat storage and limited night-time mixing exacerbate thermal discomfort and health risks. In contrast, under the moderate SSP245 pathway, where diurnal temperature peaks remain the dominant stressor, adaptation efforts should focus on reducing daytime heat exposure through shading, evaporative cooling, and reflective surfaces (Herath et al., 2018; Fabiani et al., 2019). Passive cooling strategies — such as tree-lined streets, high-albedo pavements, and water-sensitive urban design — can significantly reduce surface and air temperatures during peak hours, improving outdoor thermal comfort and reducing energy demand for cooling. These differentiated strategies highlight that the effectiveness of mitigation measures depends not only on the urban form but also on the broader climatic forcing associated with each emission pathway (Zhao et al., 2014). Moreover, the integration of climate-responsive design into urban planning is essential. Studies have shown that interventions at the neighborhood scale — such as cool roofs, permeable pavements, and strategic tree planting — can reduce urban temperatures and improve thermal comfort (Taleghani, 2018). Under SSP585, such interventions should be prioritized in areas with high nocturnal heat retention, while SSP245 scenarios may benefit more from daytime shading and albedo-enhancing materials. The observed stratification regimes also influence pollutant dispersion dynamics. Under SSP585, nocturnal stability may exacerbate pollutant accumulation near the surface, especially in densely built areas, necessitating enhanced ventilation strategies and emission control during evening hours. Conversely, under SSP245 daytime heating may promote vertical mixing but also increase ozone formation, requiring coordinated mitigation of precursor emissions (Jacob and Winner, 2009). Finally, these thermal patterns have direct implications for public health. Under SSP585, vulnerable populations — such as the elderly, children or people with pre-existing medical conditions — may face increased risks due to elevated night-time temperatures and reduced physiological recovery during sleep. In SSP245, daytime heat stress may disproportionately affect outdoor workers and children, calling for targeted adaptation measures such as cooling shelters, adjusted work schedules, and public awareness campaigns (Vicedo-Cabrera et al., 2021). Tailoring mitigation and adaptation strategies to the specific temporal characteristics of thermal stress is therefore crucial for effective urban climate resilience.

4. Conclusions

The present study examined the three-dimensional urban thermal response of the South-European city of Bologna during present and future Hot Weather (HW) events, adopting a multi-scale modeling approach. Climate projections were used to identify representative “hot years” in the near and far future under different emissions scenarios (SSP245 and SSP585). Summer months of these identified years were then downscaled using the WRF model at medium resolution to detect sub-seasonal hot weather episodes, which were subsequently simulated at high spatial resolution (0.5 km), incorporating state-of-the-art land use characterization, topography, and multilayer urban parameterization scheme to capture both horizontal and vertical thermal dynamics across urban and rural areas.

The evolution of the urban thermal structure under extreme heat conditions reveals robust and consistent features across all time periods. During HW events, urban areas experience intensified near-surface warming particularly at night, corresponding to a consistent urban–rural temperature difference of approximately 3–5° C, which highlights the exacerbation of the Urban Heat Island (UHI) effect under extreme heat conditions. Although a systematic upward shift of the 30 °C isotherm occurs, this warming is accompanied by a vertical compression of the UHI effect, which becomes shallower under more intense conditions, with its vertical extent decreasing from approximately 250 m in the present scenario to as low as 100–140 m during future HW events. These recurrent patterns (i.e. a persisting nocturnal overheating, upward displacement of heat, and reduced vertical extent of the UHI) suggest a fundamental reconfiguration of the urban boundary layer under climate stress. Compared to the present-day case, future HW events are characterized by greater thermal persistence and slower post-event recovery, especially in urban areas, highlighting the thermal inertia of built surfaces. The integrated analysis of horizontal and vertical structure, enabled by the high-resolution three-dimensional modeling framework, is a key novelty of this work, allowing for a more complete physical understanding of how extreme heat reshapes urban atmospheric stratification.

The influence of different emissions scenarios on urban thermal dynamics is substantial and structurally distinct. Under the high-emission SSP585 pathway, HW events in both near and far future scenarios lead to more intense and prolonged nocturnal UHI, greater suppression of night-time cooling, and weaker atmospheric stability, particularly in the far future where high urban temperatures persist for up to 4–5 days after the end of the HW event, compared to a 1–2 day recovery period in the present scenario. In contrast, SSP245 results in more moderate and reversible thermal anomalies, with a UHI signal that remains pronounced but follows a more regular diurnal cycle and returns more rapidly to pre-event conditions. These differences demonstrate that the choice of emissions pathway affects not only the severity of urban overheating, but also its temporal dynamics, vertical confinement, and resilience. Particularly in the far future, scenario divergence becomes more evident, confirming that mitigation efforts can meaningfully limit both the magnitude and the persistence of urban thermal stress.

The outcomes of this study are particularly relevant for historical cities in Southern Europe inland, which are (like Bologna) located in a region increasingly impacted by extreme heat events and where frequent atmospheric stagnation and weak ventilation limit nocturnal cooling and amplify heat retention. Future work should extend this study methodology to cities with contrasting ventilation regimes, such as coastal or mountainous areas, and assess how wind, humidity, and anthropogenic heat emissions modulate urban responses to extreme heat. Coupling thermal analyses with air quality and public health models would further support the development of targeted and effective urban adaptation strategies.

CRediT authorship contribution statement

Marco Possega: Writing – original draft, Visualization, Validation, Software, Methodology, Investigation, Formal analysis, Data curation, Conceptualization. **Erika Brattich:** Writing – review & editing, Writing – original draft, Supervision, Methodology, Conceptualization. **Carlo Cintolesi:** Writing – review & editing, Writing – original draft, Visualization, Supervision, Methodology, Conceptualization. **Paolo Ruggieri:** Writing – review & editing, Supervision, Methodology, Conceptualization. **Silvana Di Sabatino:** Writing – review & editing, Supervision, Resources, Project administration, Methodology, Funding acquisition, Conceptualization.

Declaration of competing interest

The authors declare that they have no known competing financial interests or personal relationships that could have appeared to influence the work reported in this paper.

Acknowledgments

This research has received funding from the European Union under grant agreement n. 101037193 (I-CHANGE project) and grant agreement n. 101057739 (TRIGGER project). The authors thank Copernicus and Regional Agency for Prevention, Environment, and Energy of Emilia Romagna (ARPAE) for providing open access data. The authors acknowledge the use of computational resources from the parallel computing cluster of the Open Physics Hub of the Department of Physics and Astronomy "Augusto Righi" at the University of Bologna (Italy).

Data availability

Data will be made available on request.

References

An, N., Dou, J., González-Cruz, J.E., Bornstein, R.D., Miao, S., Li, L., 2020. An observational case study of synergies between an intense heat wave and the urban heat island in Beijing. J. Appl. Meteorol. Clim. 59 (4), 605–620.

Anderson, B.G., Bell, M.L., 2009. Weather-related mortality: how heat, cold, and heat waves affect mortality in the united states. Epidemiology 20 (2), 205–213.

Antipova, A., 2018. Urban environment: The differences between the city in europe and the United States. In: Urban Environment, Travel Behavior, Health, and Resident Satisfaction. Springer, pp. 35–117.

Argüeso, D., Evans, J.P., Fita, L., Bormann, K.J., 2014. Temperature response to future urbanization and climate change. Clim. Dyn. 42 (7), 2183–2199.

ARPAE, 2023. Regional agency for prevention, environment and energy of emilia-romagna. https://simc.arpae.it/dext3r/. (Accessed on 15-Nov-2023).

Ascenso, A., Augusto, B., Coelho, S., Menezes, I., Monteiro, A., Rafael, S., Ferreira, J., Gama, C., Roebeling, P., Miranda, A.I., 2024. Assessing climate change projections through high-resolution modelling: A comparative study of three european cities. Sustainability 16 (17), 7276.

Barry, R.G., Chorley, R.J., 2009. Atmosphere, Weather and Climate. Routledge.

Basara, J.B., Hall Jr., P.K., Schroeder, A.J., Illston, B.G., Nemunaitis, K.L., 2008. Diurnal cycle of the oklahoma city urban heat island. J. Geophys. Res.: Atmospheres 113 (D20).

Berwal, S., Kumar, D., Pandey, A.K., Singh, V.P., Kumar, R., Kumar, K., 2016. Dynamics of thermal inertia over highly urban city: a case study of delhi. In: Remote Sensing Technologies and Applications in Urban Environments, Volume 10008. SPIE, pp. 108–114.

Bhati, S., Mohan, M., 2018. Wrf-urban canopy model evaluation for the assessment of heat island and thermal comfort over an urban airshed in india under varying land use/land cover conditions. Geosci. Lett. 5 (1), 27.

Biagi, B., Brattich, E., Cintolesi, C., Barbano, F., Di Sabatino, S., 2025. Dynamical and chemical impacts of urban green areas on air pollution in a city environment. Urban Clim. 60, 102343. http://dx.doi.org/10.1016/j.uclim.2025.102343, ISSN 2212-0955, URL https://www.sciencedirect.com/science/article/pii/S2212095525000598.

Bounoua, L., DeFries, R., Collatz, G.J., Sellers, P., Khan, H., 2002. Effects of land cover conversion on surface climate. Clim. Change 52, 29–64.

Burgstall, A., Kotlarski, S., Casanueva, A., Hertig, E., Fischer, E., Knutti, R., 2021. Urban multi-model climate projections of intense heat in switzerland. Clim. Serv. 22, 100228.

Cai, G., Du, M., 2009. Relationship between thermal inertia and urban heat sink in beijing derived from satellite images. In: 2009 Joint Urban Remote Sensing Event. IEEE, pp. 1–5.
Chew, L.W., Liu, X., Li, X.-X., Norford, L.K., 2021. Interaction between heat wave and urban heat island: A case study in a tropical coastal city, singapore. Atmos. Res. 247, 105134.
Ching, J.K., 2013. A perspective on urban canopy layer modeling for weather, climate and air quality applications. Urban Clim. 3, 13–39.
Collier, C.G., 2006. The impact of urban areas on weather. Q. J. R. Meteorol. Soc.: A J. the Atmospheric Sci. Appl. Meteorol. Phys. Ocean. 132 (614), 1–25.
Cremonini, L., Georgiadis, T., Nardino, M., Rossi, F., Rossi, A., Pinca, G., Fazzini, M., 2023. Tools for urban climate adaptation plans: A case study on bologna and outcomes for heat wave impact reduction. Challenges 14 (4), 48.
Demuzere, M., He, C., Martilli, A., Zonato, A., 2023. Technical documentation for the hybrid 100 m global land cover dataset with local climate zones for wrf.
Di Sabatino, S., Barbano, F., Brattich, E., Pulvirenti, B., 2020. The multiple-scale nature of urban heat island and its footprint on air quality in real urban environment. Atmosphere 11 (11), 1186.
Diem, P.K., Nguyen, C.T., Diem, N.K., Diep, N.T.H., Thao, P.T.B., Hong, T.G., Phan, T.N., 2024. Remote sensing for urban heat island research: Progress, current issues, and perspectives. Remote. Sens. Appl.: Soc. Environ. 33, 101081.
Doan, V.Q., Kusaka, H., 2018. Projections of urban climate in the 2050s in a fast-growing city in southeast asia: the greater ho chi minh city metropolitan area, vietnam. Int. J. Climatol. 38 (11), 4155–4171.
Eyring, V., Bony, S., Meehl, G.A., Senior, C.A., Stevens, B., Stouffer, R.J., Taylor, K.E., 2016. Overview of the coupled model intercomparison project phase 6 (cmip6) experimental design and organization. Geosci. Model. Dev. 9 (5), 1937–1958.
Fabiani, C., Pisello, A.L., Bou-Zeid, E., Yang, J., Cotana, F., 2019. Adaptive measures for mitigating urban heat islands: The potential of thermochromic materials to control roofing energy balance. Appl. Energy 247, 155–170.
Fabrizi, R., Bonafoni, S., Biondi, R., 2010. Satellite and ground-based sensors for the urban heat island analysis in the city of rome. Remote. Sens. 2 (5), 1400–1415.
Feng, J.-M., Wang, Y.-L., Ma, Z.-G., Liu, Y.-H., 2012. Simulating the regional impacts of urbanization and anthropogenic heat release on climate across china. J. Clim. 25 (20), 7187–7203.
Fernando, H., 2010. Fluid dynamics of urban atmospheres in complex terrain. Annu. Rev. Fluid Mech. 42 (1), 365–389.
Founda, D., Santamouris, M., 2017. Synergies between urban heat island and heat waves in athens (greece), during an extremely hot summer (2012). Sci. Rep. 7 (1), 10973.
Geiger, R., Aron, R.H., Todhunter, P., 2009. The Climate Near the Ground. Rowman & Littlefield.
Giannaros, T.M., Melas, D., Daglis, I.A., Keramitsoglou, I., Kourtidis, K., 2013. Numerical study of the urban heat island over athens (greece) with the wrf model. Atmos. Environ. 73, 103–111.
Gonzalez-Trevizo, M., Martinez-Torres, K., Armendariz-Lopez, J., Santamouris, M., Bojorquez-Morales, G., Luna-Leon, A., 2021. Research trends on environmental, energy and vulnerability impacts of urban heat islands: An overview. Energy Build. 246, 111051.
Hajat, S., Proestos, Y., Araya-Lopez, J.-L., Economou, T., Lelieveld, J., 2023. Current and future trends in heat-related mortality in the mena region: a health impact assessment with bias-adjusted statistically downscaled cmip6 (ssp-based) data and bayesian inference. Lancet Planet. Health 7 (4), e282–e290.
Herath, H., Halwatura, R., Jayasinghe, G., 2018. Evaluation of green infrastructure effects on tropical sri lankan urban context as an urban heat island adaptation strategy. Urban For. & Urban Green. 29, 212–222.
Hersbach, H., Bell, B., Berrisford, P., Hirahara, S., Horányi, A., Muñoz-Sabater, J., Nicolas, J., Peubey, C., Radu, R., Schepers, D., et al., 2020. The era5 global reanalysis. Q. J. R. Meteorol. Soc. 146 (730), 1999–2049.
Horton, R.M., Mankin, J.S., Lesk, C., Coffel, E., Raymond, C., 2016. A review of recent advances in research on extreme heat events. Curr. Clim. Chang. Rep. 2, 242–259.
Huang, J., Lu, X.X., Sellers, J.M., 2007. A global comparative analysis of urban form: Applying spatial metrics and remote sensing. Landsc. Urban Plan. 82 (4), 184–197.
Irfeey, A.M.M., Chau, H.-W., Sumaiya, M.M.F., Wai, C.Y., Muttil, N., Jamei, E., 2023. Sustainable mitigation strategies for urban heat island effects in urban areas. Sustainability 15 (14), 10767.
Jacob, D.J., Winner, D.A., 2009. Effect of climate change on air quality. Atmos. Environ. 43 (1), 51–63.
Jiang, S., Lee, X., Wang, J., Wang, K., 2019. Amplified urban heat islands during heat wave periods. J. Geophys. Res.: Atmospheres 124 (14), 7797–7812.
Jongen, S., Bonafè, G., 2006. Lami verification for air quality forecast and assessment purposes: case studies, special measurement campaigns, long-term evaluation. In: ARPA-SIM Internal Report.
Justice, C., Townshend, J., Vermote, E., Masuoka, E., Wolfe, R., Saleous, N., Roy, D., Morisette, J., 2002. An overview of modis land data processing and product status. Remote Sens. Environ. 83 (1–2), 3–15.
Karl, T.R., Nicholls, N., Ghazi, A., 1999. Clivar/gcos/wmo workshop on indices and indicators for climate extremes workshop summary. In: Weather and Climate Extremes: Changes, Variations and a Perspective from the Insurance Industry. pp. 3–7.
Keppas, S.C., Papadogiannaki, S., Parliari, D., Kontos, S., Poupkou, A., Tzoumaka, P., Kelessis, A., Zanis, P., Casasanta, G., de'Donato, F., et al., 2021. Future climate change impact on urban heat island in two mediterranean cities based on high-resolution regional climate simulations. Atmosphere 12 (7), 884.
Kim, S.W., Brown, R.D., 2021. Urban heat island (uhi) intensity and magnitude estimations: A systematic literature review. Sci. Total Environ. 779, 146389.
Kong, J., Zhao, Y., Carmeliet, J., Lei, C., 2021. Urban heat island and its interaction with heatwaves: A review of studies on mesoscale. Sustainability 13 (19), 10923.
Kottek, M., Grieser, J., Beck, C., Rudolf, B., Rubel, F., 2006. World map of the köppen-geiger climate classification updated. Earth Syst. Sci..
Kriegler, E., O'Neill, B.C., Hallegatte, S., Kram, T., Lempert, R.J., Moss, R.H., Wilbanks, T., 2012. The need for and use of socio-economic scenarios for climate change analysis: a new approach based on shared socio-economic pathways. Glob. Environ. Chang. 22 (4), 807–822.
Latif, M., 2013. Uncertainty in climate change projections. In: Reframing the Problem of Climate Change. Routledge, pp. 17–34.
Lee, W.V., 2014. Historical global analysis of occurrences and human casualty of extreme temperature events (etes). Nat. Hazards 70, 1453–1505.
Lemonsu, A., Viguie, V., Daniel, M., Masson, V., 2015. Vulnerability to heat waves: Impact of urban expansion scenarios on urban heat island and heat stress in paris (france). Urban Clim. 14, 586–605.
Li, D., Bou-Zeid, E., 2013. Synergistic interactions between urban heat islands and heat waves: The impact in cities is larger than the sum of its parts. J. Appl. Meteorol. Clim. 52 (9), 2051–2064.
Li, H., Zhang, H., Mamtimin, A., Fan, S., Ju, C., 2020. A new land-use dataset for the weather research and forecasting (wrf) model. Atmosphere 11 (4), 350.
Lin, C.-Y., Su, C.-J., Kusaka, H., Akimoto, Y., Sheng, Y.-F., Huang, J.-C., Hsu, H.-H., 2016. Impact of an improved wrf urban canopy model on diurnal air temperature simulation over northern taiwan. Atmospheric Chem. Phys. 16 (3), 1809–1822.
Luber, G., McGeehin, M., 2008. Climate change and extreme heat events. Am. J. Prev. Med. 35 (5), 429–435.
Ma, H., Wang, Y., Lin, Z., 2022. Future changes of summer heat waves over urban agglomerations in eastern china under 1.5 c and 2.0 c global warming. Front. Earth Sci. 10, 823286.
Ma, W., Zeng, W., Zhou, M., Wang, L., Rutherford, S., Lin, H., Liu, T., Zhang, Y., Xiao, J., Zhang, Y., et al., 2015. The short-term effect of heat waves on mortality and its modifiers in china: an analysis from 66 communities. Environ. Int. 75, 103–109.
Manoli, G., Fatichi, S., Schläpfer, M., Yu, K., Crowther, T.W., Meili, N., Burlando, P., Katul, G.G., Bou-Zeid, E., 2019. Magnitude of urban heat islands largely explained by climate and population. Nature 573 (7772), 55–60.

Mouzourides, P., Eleftheriou, A., Kyprianou, A., Ching, J., Neophytou, M.K.-A., 2019. Linking local-climate-zones mapping to multi-resolution-analysis to deduce associative relations at intra-urban scales through an example of metropolitan london. Urban Clim. 30, 100505. http://dx.doi.org/10.1016/j.uclim.2019.100505, ISSN 2212-0955. URL https://www.sciencedirect.com/science/article/pii/S2212095519302767.
Mughal, M., Li, X.-X., Norford, L.K., 2020. Urban heat island mitigation in singapore: Evaluation using wrf/multilayer urban canopy model and local climate zones. Urban Clim. 34, 100714.
Nardino, M., Cremonini, L., Crisci, A., Georgiadis, T., Guerri, G., Morabito, M., Fiorillo, E., 2022. Mapping daytime thermal patterns of bologna municipality (italy) during a heatwave: A new methodology for cities adaptation to global climate change. Urban Clim. 46, 101317.
Niu, G.-Y., Yang, Z.-L., Mitchell, K.E., Chen, F., Ek, M.B., Barlage, M., Kumar, A., Manning, K., Niyogi, D., Rosero, E., et al., 2011. The community noah land surface model with multiparameterization options (noah-mp): 1. model description and evaluation with local-scale measurements. J. Geophys. Res.: Atmospheres 116 (D12).
Nogueira, M., Lima, D.C., Soares, P.M., 2020. An integrated approach to project the future urban climate response: Changes to lisbon's urban heat island and temperature extremes. Urban Clim. 34, 100683.
Norgate, M., Tiwari, P., Das, S., Kumar, D., 2024. On the heat waves over india and their future projections under different ssp scenarios from cmip6 models. Int. J. Climatol. 44 (3), 973–995.
Oke, T., 1980. Climatic impacts of urbanization. In: Interactions of Energy and Climate: Proceedings of an International Workshop Held in MÜnster, Germany. vol. 3–6, Springer, pp. 339–361.
Oke, T.R., Mills, G., Christen, A., Voogt, J.A., 2017. Urban Climates. Cambridge University Press.
Perkins, S.E., 2015. A review on the scientific understanding of heatwaves—their measurement, driving mechanisms, and changes at the global scale. Atmos. Res. 164, 242–267.
Perkins, S.E., Alexander, L., Nairn, J., 2012. Increasing frequency, intensity and duration of observed global heatwaves and warm spells. Geophys. Res. Lett. 39 (20).
Phelan, P.E., Kaloush, K., Miner, M., Golden, J., Phelan, B., H. Silva, I.I.I., Taylor, R.A., 2015. Urban heat island: mechanisms, implications, and possible remedies. Annu. Rev. Environ. Resour. 40 (1), 285–307.
Pielke Sr, R.A., Pitman, A., Niyogi, D., Mahmood, R., McAlpine, C., Hossain, F., Goldewijk, K.K., Nair, U., Betts, R., Fall, S., et al., 2011. Land use/land cover changes and climate: modeling analysis and observational evidence. Wiley Interdiscip. Rev.: Clim. Chang. 2 (6), 828–850.
Possega, M., Aragão, L., Ruggieri, P., Santo, M.A., Di Sabatino, S., 2022. Observational evidence of intensified nocturnal urban heat island during heatwaves in european cities. Environ. Res. Lett. 17 (12), 124013.
Qiao, Z., Wang, N., Chen, J., Xu, X., Liu, L., Han, D., 2024. Understanding the differences in the contribution and impact of urbanization on urban warming during heatwave and non-heatwave periods in china. J. Clean. Prod. 474, 143626.
Rafael, S., Martins, H., Sá, E., Carvalho, D., Borrego, C., Lopes, M., 2016. Influence of urban resilience measures in the magnitude and behaviour of energy fluxes in the city of porto (portugal) under a climate change scenario. Sci. Total Environ. 566, 1500–1510.
Richard, Y., Pohl, B., Rega, M., Pergaud, J., Thévenin, T., Emery, J., Dudek, J., Vairet, T., Zito, S., Chateau-Smith, C., 2021. Is urban heat island intensity higher during hot spells and heat waves (dijon, france, 2014–2019)? Urban Clim. 35, 100747.
Roberge, F., Sushama, L., 2018. Urban heat island in current and future climates for the island of montreal. Sustain. Cities Soc. 40, 501–512.
Robinson, P.J., 2001. On the definition of a heat wave. J. Appl. Meteorol. Clim. 40 (4), 762–775.
Rosenzweig, C., Solecki, W.D., Parshall, L., Chopping, M., Pope, G., Goldberg, R., 2005. Characterizing the urban heat island in current and future climates in new jersey. Glob. Environ. Chang. Part B: Environ. Hazards 6 (1), 51–62.
Rossa, A.M., Ferrario, M.E., Sansone, M., Monai, M., 2020. Climatology of the static stability of the night-time po valley pbl from radio sondes and passive microwave radiometers. In: Technical Report. CETEMPS.
Salamanca, F., Krpo, A., Martilli, A., Clappier, A., 2010. A new building energy model coupled with an urban canopy parameterization for urban climate simulations—part i, formulation, verification, and sensitivity analysis of the model. Theor. Appl. Climatol. 99 (3), 331–344.
Salamanca, F., Zhang, Y., Barlage, M., Chen, F., Mahalov, A., Miao, S., 2018. Evaluation of the wrf-urban modeling system coupled to noah and noah-mp land surface models over a semiarid urban environment. J. Geophys. Res.: Atmospheres 123 (5), 2387–2408.
Sandstad, M., Schwingshackl, C., Iles, C., 2022. Climate extreme indices and heat stress indicators derived from cmip6 global climate projections. Copernicus Climate Change Service (C3S) Climate Data Store (CDS, http://dx.doi.org/10.24381/cds.776e08bd, (Accessed on 15-Nov-2023).
Santamouris, M., 2014. Cooling the cities–a review of reflective and green roof mitigation technologies to fight heat island and improve comfort in urban environments. Sol. Energy 103, 682–703.
Sarangi, C., Qian, Y., Li, J., Leung, L.R., Chakraborty, T., Liu, Y., 2021. Urbanization amplifies nighttime heat stress on warmer days over the us. Geophys. Res. Lett. 48 (24), e2021GL095678.
Scott, A.A., Waugh, D.W., Zaitchik, B.F., 2018. Reduced urban heat island intensity under warmer conditions. Environ. Res. Lett. 13 (6), 064003.
Sharma, R., Hooyberghs, H., Lauwaet, D., De Ridder, K., 2019. Urban heat island and future climate change—implications for delhi's heat. J. Urban Health 96, 235–251.
Shukla, P.R., Skea, J., Slade, R., Al Khourdajie, A., van Diemen, R., McCollum, D., Pathak, M., Some, S., Vyas, P., Fradera, R., et al., 2022. Climate change 2022: Mitigation of climate change. Contrib. Work. Group III To Sixth Assess. Rep. Intergov. Panel Clim. Chang. 10 (2022), 9781009157926.
Siewert, J., Kroszczynski, K., 2020. Gis data as a valuable source of information for increasing resolution of the wrf model for warsaw. Remote. Sens. 12 (11), 1881.
Silva, R., Carvalho, A.C., Pereira, S.C., Carvalho, D., Rocha, A., 2022. Lisbon urban heat island in future urban and climate scenarios. Urban Clim. 44, 101218.
Stefanon, M., D'Andrea, F., Drobinski, P., 2012. Heatwave classification over europe and the mediterranean region. Environ. Res. Lett. 7 (1), 014023.
Straffelini, E., Tarolli, P., 2023. Climate change-induced aridity is affecting agriculture in northeast italy. Agricult. Sys. 208, 103647.
Taleghani, M., 2018. Outdoor thermal comfort by different heat mitigation strategies-a review. Renew. Sustain. Energy Rev. 81, 2011–2018.
Tapiador, F.J., Navarro, A., Moreno, R., Sánchez, J.L., García-Ortega, E., 2020. Regional climate models: 30 years of dynamical downscaling. Atmos. Res. 235, 104785.
Tewari, M., Yang, J., Kusaka, H., Salamanca, F., Watson, C., Treinish, L., 2019. Interaction of urban heat islands and heat waves under current and future climate conditions and their mitigation using green and cool roofs in new york city and phoenix, arizona. Environ. Res. Lett. 14 (3), 034002.
Theeuwes, N.E., Steeneveld, G.-J., Ronda, R.J., Holtslag, A.A., 2017. A diagnostic equation for the daily maximum urban heat island effect for cities in northwestern europe. Int. J. Climatol. 37 (1), 443–454.
Tong, S., Wang, X.Y., Barnett, A.G., 2010. Assessment of heat-related health impacts in brisbane, australia: comparison of different heatwave definitions. PloS One 5 (8), e12155.
Valmassoi, A., Dudhia, J., Di Sabatino, S., Pilla, F., 2020. Irrigation impact on precipitation during a heatwave event using wrf-arw: The summer 2015 po valley case. Atmos. Res. 241, 104951.
Vicedo-Cabrera, A.M., Scovronick, N., Sera, F., Royé, D., Schneider, R., Tobias, A., Astrom, C., Guo, Y., Honda, Y., Hondula, D., et al., 2021. The burden of heat-related mortality attributable to recent human-induced climate change. Nat. Clim. Chang. 11 (6), 492–500.
Vogel, J., Afshari, A., 2020. Comparison of urban heat island intensity estimation methods using urbanized wrf in berlin, germany. Atmosphere 11 (12), 1338.
Voogt, J.A., Oke, T.R., 2003. Thermal remote sensing of urban climates. Remote Sens. Environ. 86 (3), 370–384.

Wang, D., Lau, K.K.-L., Ren, C., Goggins, W.B.I., Shi, Y., Ho, H.C., Lee, T.-C., Lee, L.-S., Woo, J., Ng, E., The impact of extremely hot weather events on all-cause mortality in a highly urbanized and densely populated subtropical city: A 10-year time-series study (2006–2015). Sci. Total Environ. 690 (2019), 923–931.
Whiteman, C.D., 2000. Mountain Meteorology: Fundamentals and Applications. Oxford University Press.
WMO, W., 2015. Heat waves and health: guidance on warning-system development. http://www.who.int/globalchange/publications/heatwaveshealth-guidance/en. (Accessed, 12 2015).
Xu, Y., Dadvand, P., Barrera-Gómez, J., Sartini, C., Marí-Dell'Olmo, M., Borrell, C., Medina-Ramón, M., Sunyer, J., Basagaña, X., 2013. Differences on the effect of heat waves on mortality by sociodemographic and urban landscape characteristics. J. Epidemiol. Community Health 67 (6), 519–525.
Xu, Z., Han, Y., Tam, C.-Y., Yang, Z.-L., Fu, C., 2021. Bias-corrected cmip6 global dataset for dynamical downscaling of the historical and future climate (1979–2100). Sci. Data 8 (1), 293.
Yang, J., Wang, Z.-H., 2015. Optimizing urban irrigation schemes for the trade-off between energy and water consumption. Energy Build. 107, 335–344.
Zeng, W., Lao, X., Rutherford, S., Xu, Y., Xu, X., Lin, H., Liu, T., Luo, Y., Xiao, J., Hu, M., et al., 2014. The effect of heat waves on mortality and effect modifiers in four communities of guangdong province, china. Sci. Total Environ. 482, 214–221.
Zhang, K., Chen, T.-H., Begley, C.E., 2015. Impact of the 2011 heat wave on mortality and emergency department visits in houston, texas. Environ. Health 14 (1), 11.
Zhao, L., Lee, X., Smith, R.B., Oleson, K., 2014. Strong contributions of local background climate to urban heat islands. Nature 511 (7508), 216–219.
Zhao, L., Oppenheimer, M., Zhu, Q., Baldwin, J.W., Ebi, K.L., Bou-Zeid, E., Guan, K., Liu, X., 2018. Interactions between urban heat islands and heat waves. Environ. Res. Lett. 13 (3), 034003.
Zhu, D., Ooka, R., 2023. Wrf-based scenario experiment research on urban heat island: A review. Urban Clim. 49, 101512.
Zonato, A., Martilli, A., Di Sabatino, S., Zardi, D., Giovannini, L., 2020. Evaluating the performance of a novel wudapt averaging technique to define urban morphology with mesoscale models. Urban Clim. 31, 100584.